Ca 2+ handling remodeling and STIM1L/Orai1/TRPC1/TRPC4 upregulation in monocrotaline-induced right ventricular hypertrophy

Jessica Sabourin, Boet Angèle, Rucker-Martin Catherine, Lambert Mélanie, Ana-Maria Gomez, Benitah Jean-Pierre, Perros Frédéric, Humbert Marc, Fabrice Antigny

Ca^{2+} handling remodeling and STIM1L/Orai1/TRPC1/TRPC4 upregulation in monocrotaline-induced right ventricular hypertrophy

Sabourin Jessica[1], Boet Angèle[2,3,4] Rucker-Martin Catherine[2,3,4], Lambert Mélanie[2,3,4], Gomez Ana-Maria[1], Benitah Jean-Pierre[1], Humbert Marc[2,3,4], Perros Frédéric[2,3,4] and Antigny Fabrice[2,3,4]

[1]Signalisation et Physiopathologie Cardiovasculaire - UMR-S 1180, Univ. Paris-Sud, INSERM, Université Paris-Saclay, 92296, Châtenay-Malabry, France

[2] Univ. Paris–Sud, Faculté de Médecine, Université Paris-Saclay, Le Kremlin Bicêtre, France

[3]Assistance Publique Hôpitaux de Paris, Service de Pneumologie, Hôpital Bicêtre, Le Kremlin Bicêtre, France

[4]Inserm UMR_S 999, Hôpital Marie Lannelongue, Le Plessis Robinson, France

Corresponding author: Fabrice Antigny, INSERM UMR_S 999, Hôpital Marie Lannelongue, 133, Avenue de la Résistance, F-92350 Le Plessis Robinson, France. Fax: (33) 1 40 94 25 22, Tel.: (33) 1 40 94 25 15, e-mail: fabrice.antigny@u-psud.fr

Abstract

Background Right ventricular (RV) function is the most important prognostic factor for pulmonary arterial hypertension (PAH) patients. The progressive increase of pulmonary vascular resistance induces RV hypertrophy (RVH) and at term RV failure (RVF). However, the molecular mechanisms of RVH and RVF remain understudied. In this study, we gained insights into cytosolic Ca^{2+} signaling remodeling in ventricular cardiomyocytes during the pathogenesis of severe pulmonary hypertension (PH) induced in rats by monocrotaline (MCT) exposure, and we further identified molecular candidates responsible for this Ca^{2+} remodeling.

Methods and Results After PH induction, hypertrophied RV myocytes presented longer action potential duration, higher and faster $[Ca^{2+}]_i$ transients and increased sarcoplasmic reticulum (SR) Ca^{2+} content, whereas no changes in these parameters were detected in left ventricular (LV) myocytes. These modifications were associated with increased P-Ser^{16}-phospholamban pentamer expression without altering SERCA2a (Sarco/Endoplasmic Reticulum Ca^{2+}-ATPase) pump abundance. Moreover, after PH induction, Ca^{2+} sparks frequency were higher in hypertrophied RV cells, while total RyR2 (Ryanodine Receptor) expression and phosphorylation were unaffected. Together with cellular hypertrophy, the T-tubules network was disorganized. Hypertrophied RV cardiomyocytes from MCT-exposed rats showed decreased expression of classical STIM1 (Stromal Interaction molecule) associated with increased expression of muscle-specific STIM1 Long isoform, glycosylated-Orai1 channel form, and TRPC1 and TRPC4 channels, which was correlated with an enhanced Ca^{2+}-release-activated Ca^{2+} (CRAC)-like current. Pharmacological inhibition of TRPCs/Orai1 channels in hypertrophied RV cardiomyocytes normalized $[Ca^{2+}]_i$ transients amplitude, the SR Ca^{2+} content and cell contractility to control levels. Finally, we showed that most of these changes did not appear in LV cardiomyocytes.

Conclusions These new findings demonstrate RV-specific cellular Ca^{2+} cycling remodeling in PH rats with maladaptive RVH and that the STIM1L/Orai1/TRPC1/C4-dependent Ca^{2+} current participates in this Ca^{2+} remodeling in RVH secondary to PH.

Keywords $[Ca^{2+}]_i$ transients, STIM1L, Orai1, TRPCs, right ventricular hypertrophy, pulmonary hypertension, monocrotaline rat

Introduction

Pulmonary arterial hypertension (PAH) is a progressive and lethal cardiopulmonary disease defined by an increased mean pulmonary artery pressure (mPAP) (≥25 mmHg at rest) with a normal pulmonary capillary wedge pressure (<15 mmHg) and by high pulmonary vascular resistance (>3 Wood units) [1]. Increased right ventricular (RV) afterload leads to RV hypertrophy (RVH) and RV failure (RVF) [2]. RVF is the most important prognostic factor for morbidity and mortality in PAH or pulmonary hypertension (PH) secondary to left heart disease [3,4]. Surprisingly, the RV is not targeted by PAH-specific therapies. The current deep lack of basic understanding regarding PAH-related RV remodeling can, at least in part, explain this paradox. Moreover, extrapolating the abundant knowledge derived from studies on left ventricular hypertrophy (LVH) to studies on RVH is not possible. The two ventricles have many differences, including different embryologic origins. The RV and RV outflow tract are derived from the anterior heart field, whereas the LV and the atrial chambers are derived from the primary heart field [5]. On the other hand, the primary function of the RV is to receive systemic venous return and to drive blood into the pulmonary arteries. Therefore, the physiology and hemodynamic function of the RV under normal condition differ considerably from those of the LV, and the known mechanisms of LV dysfunction cannot be generalized to RV dysfunction [4].

In the LV, cardiac adaptation to various pathological stresses is linked to molecular remodeling of sarcoplasmic reticulum (SR) Ca^{2+} cycling. A hallmark of heart failure is pathological hypertrophy, which is thought to be an initial compensatory response of the heart to an increased workload to maintain heart function. However, with a sustained hemodynamic load, maladaptive cardiac hypertrophy leads to LV dilation, loss of cardiomyocytes, progressive fibrosis, and cardiac dysfunction. At the molecular level, pathological LVH and LV failure (LVF) are commonly associated with reduced contractility due to altered excitation-contraction coupling (ECC) function [6]. Reductions in $[Ca^{2+}]_i$ transients magnitude and contraction in failing cells largely result from 1) decreased SR Ca^{2+} content due to reduced sarco-endoplasmic reticulum Ca^{2+} ATPase 2a (SERCA2a) expression [7] and/or increased ryanodine receptor (RyR) leakage [8], 2) increased Na^+/Ca^{2+} exchanger (NCX) expression [9] and 3) impaired efficacy of the L-type Ca^{2+} channel current to trigger Ca^{2+} release [10] due to T-tubule disorganization [11].

The severe PH induced in rats by monocrotaline (MCT) exposure (MCT-PH model) reproduces many of the cellular and molecular events that occur during the pathogenesis of RVH related to PH and ultimately lead to lethal RVF [12].

In the MCT-PH model, prolonged action potentials have been described in the RV, supporting altered Ca^{2+} handling. Indeed, early studies using aequorin bioluminescence have shown that MCT-treated rats with compensated RVH display prolonged isovolumic contraction due to a decreased rate of Ca^{2+} sequestration [13,14]. By contrast, enhanced Ca^{2+} mobilization and sequestration during contraction/relaxation cycles has been found in the early stage of RVH [15]. In severe RVH with congestive heart failure, RV myocytes from MCT-exposed rats have smaller and slower $[Ca^{2+}]_i$ transients with a decreased density of SR, which is consistent with data from experimental models of LVF [15,16]. Conversely, an increase in $[Ca^{2+}]_i$ transients amplitude and cell shortening associated with a higher SR Ca^{2+} load in failing myocytes from MCT-PH rats have also been reported [17]. These

discrepancies and the limited research in RV Ca^{2+} remodeling warrant further investigations to clarify and to deepen our understanding of the role of Ca^{2+} signaling in PH-related RV remodeling. This knowledge could allow the identification of new key mediators of RVH and RVF pathogenesis and the development of heart-targeting innovative therapeutic strategies for PAH.

Recently, Store-Operated Ca^{2+} entry (SOCE) has been reported to participate in Ca^{2+} influx in cardiac cells. Although its role in non-excitable cells is well established, its function in cardiac physiology is unclear. SOCE has three essential components: the regulatory element belonging to the stromal interaction molecule family STIM (STIM1-2) and two Store-Operated Ca^{2+} channels (SOCs), namely, TRPCs (Transient Receptor Potential Canonical 1-7) and Orai (Orai1-3) [18,19]. STIM1 acts as the endoplasmic/sarcoplasmic reticulum (ER/SR) Ca^{2+} sensor and communicates information regarding the stored Ca^{2+} content to initiate Orai- and/or TRPCs-mediated SOCE.

We and others have proposed that SOCE plays a role in maintaining diastolic Ca^{2+} homeostasis in LV myocytes over time under unstressed conditions and is crucial for postnatal cardiac growth [20–22]. Moreover, during the last decade, several studies have reported strong evidence for the roles of STIM1, Orai1/3 and TRPCs in the altered Ca^{2+} signaling underlying the development of LVH and LVF, implying re-induction of the fetal gene program governed by calcineurin/NFAT (Nuclear factor of activated T-cells) signaling, a feature of stressed cardiomyocytes. Indeed, TRPC1, -C3, -C6, -C7, Orai1, STIM1 and Orai3 have been reported to be upregulated in several animal models of LVH or LVF [23–30]. However, the contributions of TRPCs, Orai and STIM proteins to RVH secondary to PH remain unknown.

In the current study, we combine *in vivo* cardiac function investigations with biochemical analyses and functional *in vitro* studies by patch-clamp and confocal Ca^{2+} imaging to 1) gain insights into the intrinsic Ca^{2+} cycling properties of RV and LV adult cardiomyocytes and 2) further identify molecular candidates responsible for Ca^{2+} remodeling during the development of RV dysfunction in the context of severe PH. Our findings demonstrate RV-specific cellular Ca^{2+} cycling remodeling in experimental maladaptive RVH and the contribution of STIM1 Long isoform and the Orai1/TRPCs-dependent Ca^{2+} current to this $[Ca^{2+}]_i$ remodeling.

Material and methods

Chemicals

Nifedipine, caffeine and monocrotaline (MCT) were obtained from Sigma-Aldrich (France). KB-R7943 and BTP-2 were obtained from TOCRIS (United Kingdom). Fluo-4/AM and Di-4-ANEPPS (Pyridinium, 4-(2-(6-(dibutylamino)-2-naphthalenyl) ethenyl)-1-(3-sulfopropyl)-, hydroxide) were obtained from Thermo Fisher Scientific (France).

Animals

Rats were housed at the AnimEX platform, Châtenay Malabry, France. The experiments were conducted according to the European Union regulations (Directive 86/609 EEC) for animal experiments and complied with our institution's guidelines for animal care and handling. The animal facility is licensed by the French Ministry of

Agriculture (agreement N° B92-019-01). This study was approved by the Committee on the Ethics of Animal Experiments CEEA26 CAP Sud and the agreement delivered by the French Ministry of Agriculture for animal experiments. Male Wistar rats (100–150 g) (Janvier SAS, France) were maintained in a temperature-controlled room with a 12:12-h light–dark cycle.

Monocrotaline (MCT)-induced pulmonary hypertension

PH was induced in Wistar rats by a single subcutaneous injection of MCT (60 mg/kg) and the control rats were injected with saline solution [31]. The animals were evaluated at various time points after MCT administration (1, 2 and 3 weeks).

Evaluation of right ventricular hypertrophy (RVH)

For Fulton's index of RVH, the ratio of right ventricular weight to left ventricular plus septal weight (RV/LV+S) was calculated.

Echocardiographic evaluation of RV and LV function

Trans-thoracic echocardiography (TTE) was performed with a digital ultrasound system (Vivid E9, GE Healthcare) using a high-frequency phased array transducer (12 S-D 4-12MHz, GE Healthcare). The echocardiographic evaluation was performed under general anesthesia with the rats breathing spontaneously using an Isoflurane Rodent Anesthesia System (Minerve, Esternay, France) (induction: isoflurane 3% in room air; maintenance: isoflurane 2% in room air). The rats were shaved and body temperature was maintained during TTE. The time under anesthesia was short enough (less than 15 minutes) to minimize the effect of isoflurane. TTE examinations were all performed by the same trained operator in a blinded fashion to avoid inter-operator variability. The Pulsed Wave Doppler region of interest was 1.5 mm, the gain value was high and the frame rate was maximized. Data analyses were performed directly or offline with EchoPac Software (GE Medical).
Echocardiography was performed at baseline W0 (before MCT injection), W1, W2 and W3 (1, 2 and 3 weeks after injection) under the same condition. Measurements were all performed in triplicate (all data were averaged during 5 cardiac cycles) and the following parameters were analyzed:
In the parasternal short-axis view: pulmonary artery acceleration time (PAAT), cycle length with heart rate (HR) and the pulmonary artery velocity time integral (VTI pulmonary artery).
In the 4-cavity view performed in the subcostal view, we measured RV and LV thickness, RV or LV end diastolic diameter (RV EDd, LV EDd, respectively) and systolic diameter (RV EDs, LV EDd) and interventricular septum deviation.
These data were assessed according to guidelines for RV and LV echocardiographic measurements [26]. RV and LV fractional shortening (FS) correspond to the percent change in LV and RV cavity diameters, respectively. LV FS (%) = ((LV EDd-LV EDs)/LV EDd)*100 or RV FS (%) = ((RV EDd-RV EDs)/RV EDd)*100.

Isolation of adult rat ventricular myocytes

Excised hearts were mounted on a Langendorff apparatus and perfused through the coronaries for 40 to 50 min with collagenase A (Roche, Meylan, France) in a Hanks-HEPES buffer solution containing (in mM): NaCl, 117; KCl, 5.7; $MgCl_2$, 1.7; KH_2PO_4, 1.5; $NaHCO_3$, 4.4; HEPES, 21; glucose, 11.7; creatine, 10; and taurine, 20, and bubbled with 100% O_2, pH 7.1. At the end of enzymatic digestion, the RV and LV were separated, chopped finely and agitated manually to dissociate individual myocytes. A proportion of the freshly isolated cells was used for Ca^{2+} imaging and patch-clamp experiments, and the other proportion was frozen for subsequent Western-blot or quantitative RT-PCR analyses.

Measurement of $[Ca^{2+}]_i$ transients and the SR Ca^{2+} load

Fresh RV and LV cardiomyocytes were incubated for 30 min at room temperature with 7 µM of Fluo-4/AM. The Fluo-4 Ca^{2+} signal was recorded with a laser scanning confocal microscope (Leica SP5) equipped with a ×40 water immersion objective. Fluo-4 was excited at 490 nm with a white light laser, and emission was collected at >510 nm. The cardiomyocytes, which were continuously perfused with physiological saline solution, were paced at 1 Hz. $[Ca^{2+}]_i$ transients were recorded by scanning the cells in Xt line mode. The cytosolic Ca^{2+} variation was normalized by dividing the peak fluorescence intensity (F) by the average resting fluorescence intensity (F_0) to generate an F/F_0 image after background subtraction. The following $[Ca^{2+}]_i$ transients properties were evaluated from the F/F_0 fluorescence trace: peak F/F_0 and the time constant of decay (ms), which was calculated by fitting the decay portion of the fluorescence trace to a monoexponential function. For SR Ca^{2+} load estimation, cardiomyocytes were rapidly perfused with 10 mM caffeine immediately after field stimulation. The amplitude of the caffeine-evoked $[Ca^{2+}]_i$ transients was used to assess the SR Ca^{2+} load. Fractional SR release was measured by normalizing the steady state of $[Ca^{2+}]_i$ transients (peak F/F_0) by caffeine-evoked $[Ca^{2+}]_i$ transients. Post-rest potentiation was calculated by normalizing the first $[Ca^{2+}]_i$ transients (peak F/F_0) after a period of rest to reach the steady-state $[Ca^{2+}]_i$ transients.

Ca^{2+} sparks were recorded in quiescent cells and the properties of amplitude (F/F_0), duration (FDHM, full duration at half maximum, in ms) and width (FWHM, full width at half maximum, in µm) were measured. Images of Ca^{2+} sparks were normalized by dividing the fluorescence intensity of each pixel (F) by the average resting fluorescence intensity (F_0) to generate an F/F_0 image. All $[Ca^{2+}]_i$ transients and Ca^{2+} spark parameters were analyzed with IDL 8.6 software.

Electrophysiological recordings

Action potentials, membrane currents and cell membrane capacitance were recorded by the whole-cell patch-clamp technique at room temperature (22–24°C) with the Axopatch 200B amplifier, the Digidata 1440A, and pClamp 10 software (Molecular Devices, Sunnyvale, CA, USA). Borosilicate glass pipettes (Harvard Apparatus) were pulled with a Sutter puller, fired, and polished and had a resistance between 2.5-3.5 MΩ. Series resistance was electronically compensated up to 50% and was continually monitored during the experiment. Membrane capacitance was measured for each cell with pClamp 10 software.

To record action potentials, cells were perfused with an external solution containing (in mM): NaCl, 140; KCl, 5.4; $CaCl_2$, 1.5; $MgCl_2$, 1.2; HEPES, 10; glucose, 11 (pH 7.4 NaOH), while the pipette solution had the following composition (in mM): K-aspartate, 130; KCl, 10; NaCl, 7; $MgCl_2$, 1.2; ethyleneglycol-bis-(fl-aminoethylether), EGTA, 0.1; HEPES, 10 (pH 7.2 with NaOH).
For I_{CRAC}-like current recording, the pipette solution contained (in mM): CsCl, 135; $MgCl_2$, 4; EGTA, 5; HEPES, 10 Na_2 ATP, 5; and Na_2 creatine phosphate, 3; (pH 7.2 with LiOH), and cells were perfused with a solution containing in mM: NaCl, 132; $MgCl_2$, 1.1; CsCl, 4; $CaCl_2$ 10; glucose, 10; nifedipine, 0.01; KB-R7943, 0.05 and HEPES, 10; (pH 7.4 with LiOH). The I_{CRAC}-like current was elicited by a 1.2-s voltage ramp from +60 to -120 mV to inactivate the voltage-dependent Na^+ channels.

Quantitative-PCR

Total RNA from isolated cardiomyocytes was extracted by the classic Trizol procedure. One microgram of total RNA was reverse-transcribed using the QuantiTect reverse Transcription Kit (Qiagen, Hilden, Germany) as previously described (Lambert M et al., Cardiovasc Research 2018). The results were analyzed with the $2^{-\Delta\Delta CT}$ method. The primers used in this study are listed in Table 2.

Western-blot analysis

The western-blot protocol was previously described [2] and the antibodies used are listed in Table 3.

Immunofluorescence Staining

Isolated cardiomyocytes were fixed with methanol for 10 min at -20°C. Slices were saturated with rat (10%) and donkey (10%) sera in PBS for 1 hour at room temperature. Mouse monoclonal anti-RyR2 (1/100, Table 3) was incubated for 1 hour at room temperature. DAPI was used to stain nuclei.
Micro-vessel density was expressed as the percentage of CD31 (anti-CD31 1/10)-stained cells measured in the whole section.
Sections were viewed under an LSM 700 microscope (Carl Zeiss, Le Pecq, France) equipped with 405- and 488-nm lasers (Carl Zeiss). Images were recorded and analyzed with ZEN software (Carl Zeiss).

Histological assessment

Hearts were fixed in 4% paraformaldehyde, paraffin embedded and serially sectioned (5 µm). The sections were stained with Sirius red (0.1%) to evaluate fibrosis as a percentage of the total tissue area.

T-tubule imaging and analysis

After plating on laminin, myocytes were loaded with the lipophilic membrane marker Di-4-ANEPPS (Pyridinium, 4-(2-(6-(dibutylamino)-2-naphthalenyl) ethenyl)-1-(3-sulfopropyl)-, hydroxide) 2 µM in a Ringer solution for 10

min). After washout, T-tubules were examined using a confocal microscope (LSM700, Carl Zeiss, Le Pecq, France) with a 40x NA 1.30 oil immersion objective and the pinhole set to 1 Airy unit. Di-4-ANEPPS was excited at 478 nm and fluorescence was collected between 550 and 750 nm. T-tubule quantification was performed using ImageJ software.

Statistical analysis

All values are expressed as the mean ± SEM. For all experiments, the difference between two groups was assessed with two-tailed unpaired or paired Student's *t*-test and between at least four groups with one-way or two-way ANOVA completed by Fisher LSD's *post hoc* or by Kruskal-Wallis test for multiple comparisons. For echocardiography analyses, we performed Mann Whitney's *t*-test between Control W1 *vs.* MCT W1, Control W2 *vs.* MCT W2 and Control W3 *vs.* MCT W3. Differences were considered statistically significant at $*P<0.05$, $**P<0.01$, and $***P<0.001$. All statistical tests were performed with GraphPad Prism software (GraphPad, version 6.0 for Windows).

Results

Progressive development of RVH and dysfunction associated with capillary rarefaction, fibrosis and inflammation in MCT-PH rats

To assess the time course of RV and LV cardiac function in MCT-exposed rats, serial echocardiography from anesthetized animals was performed during the development of PH (Table 1). In accordance with our previous data demonstrating increased mean pulmonary arterial pressure (PAP) by RV catheterization at W2 and W3 after MCT exposure [32], we confirmed the establishment of PH by progressive shortening of pulmonary artery acceleration time (PAAT) and a decreased velocity-time integral (VTI) in MCT rats (W2 and W3) compared to their respective controls (Table 1). We also evaluated the degree of RVH by the Fulton index (RV to (LV) + Septum (S)) weight ratio) and observed a progressive and significant increase in RV mass 2 and 3 weeks after MCT (Table 1).

At W2, the RV wall thickness was slightly increased compared to that in the control rats, reflecting RVH without any alterations in cardiac function. By contrast, one week later, we found a strong increase in RV wall thickness, marked RV dilatation with an increase in the RV end diastolic parameter and a severe decline in RV function as measured by fractional shortening (FS) (Table 1).

Concerning LV function in MCT-PH rats, we measured significant reductions in the aorta VTI, LV end diastolic and end systolic diameters (LV EDd and EDs) and LV thickness only 3 weeks after MCT exposure (Table 1). However, the LV showed conserved contractility as shown by preserved FS. Finally, the cardiac output (CO) and cardiac index (CI) were reduced at W3 in the MCT rats (Table 1). Additionally, due to RVH, we observed an interventricular septum curve deviation of type 2 (flat) or type 3 (right to left deviation) and tricuspid valve leak at W3 (data not shown). Taken together, these data demonstrate progressive RVH in MCT-exposed rats beginning at W2, with a rapid decline in RV function in MCT-exposed rats over 3 weeks predictive of a maladaptive form of RVH.

We also showed that vessel density (using immunostaining against CD31 (Fig.1a) and western-blotting against CD31 and CD34 (Fig.1b) as endothelium markers) was substantially reduced in RV tissues from MCT-PH rats compared to that in control rats. Three weeks after PH induction, we also measured a strong increase in RV fibrosis (quantified by Sirius red staining) (Fig.1c) correlated with significant induction of fibrotic markers such as *Col1a1* and *Col3a1* at the mRNA level (Fig.1d). Then, we evaluated the RV inflammatory status by analyzing CD45 (a pan leukocyte marker) protein expression. We showed a progressive increase in CD45 protein expression from W2 until W3, revealing the presence of inflammatory cells in RV tissues from MCT-PH rats (Supplemental Fig. 1). These observations indicated that RV capillary rarefaction, fibrosis and inflammation could contribute to RV dysfunction in MCT-PH rats.

RVH was confirmed at the cellular level by measuring cell membrane capacitance by patch-clamp in freshly isolated adult RV cardiomyocytes from MCT rats at W2 and W3 (Fig. 2a), while cell capacitance was unchanged at W1 and in LV myocytes from MCT rats at any time point (Supplemental Fig. 2a). Using the whole-cell patch-clamp technique, we showed that cell hypertrophy was associated with progressive prolongation of action potential at 20%, 50% and 90% of the repolarizing phase (Fig. 2b) as we previously observed [33], demonstrating abnormal action potential repolarization in RV cardiomyocytes isolated from MCT-PH rats.

Three weeks after PH induction, we also observed a switch of myosin heavy chain (MHC) isoforms from α (adult-*MYH6*) to β (fetal-*MYH7*) in RV cardiomyocytes (Fig. 2c). This switch was confirmed at the protein level in RV tissues from MCT-PH rats (Fig. 2d-e). In LV cardiomyocytes, we measured an increase in the *MYH7* mRNA level at W3 without any induction of β-MHC protein expression (Supplemental Fig. 2b-c). The mRNA level of *MYH6* in LV cardiomyocytes was unchanged 3 weeks after PH induction as well as α-MHC protein expression (Supplemental Fig. 1b-c). Moreover, we showed increases in the expression levels of pro-hypertrophic markers such as atrial natriuretic factor (ANF, encoded by *Nppa*) and B-type natriuretic peptide (BNP, encoded by *Nppb*) at W3 in RV cardiomyocytes (Fig. 2f-g), confirming the hypertrophic phenotype of the RV. *Nppb*, but not *Nppa*, is also enhanced in LV myocytes after 3 weeks of MCT exposure (Supplemental Fig. 2d).

Increased $[Ca^{2+}]_i$ transients and cell shortening in hypertrophied RV myocytes

We hypothesized that altered RV Ca^{2+} handling may contribute to RVH and RV dysfunction after PH establishment. We analyzed electrically-evoked $[Ca^{2+}]_i$ transients and cell shortening in isolated adult RV and LV cardiomyocytes from control rats (control) and MCT-PH rats (at W1, W2 and W3 after MCT injection). Figure 3a shows representative line-scan images (top panel) and corresponding fluorescence traces (bottom panel) of Fluo-4-loaded cells from control RV cardiomyocytes (a) and RV cardiomyocytes at W1 (b), W2 (c) and (d) W3 after MCT exposure upon field stimulation at 1 Hz. Notably, all results from the control rats (at W1, W2, and W3) were pooled because of similar Ca^{2+} cycling properties. $[Ca^{2+}]_i$ transients amplitudes were unchanged at W1 and W2, but they were significantly increased at W3 (Fig. 3b). Moreover, $[Ca^{2+}]_i$ transients decay time was significantly shortened in RV myocytes at W3 (Fig. 3c), suggesting faster Ca^{2+} uptake by the SERCA pump.
Importantly, the increase in $[Ca^{2+}]_i$ transients amplitudes was associated with an increase in cell shortening in RV myocytes at W3 (Fig. 3d). Notably, no significant modifications were detected in LV cardiomyocytes (Fig. 3b-d). SERCA2a activity depends on Ca^{2+} levels and protein expression of SERCA2a and its endogenous inhibitor, phospholamban (PLB). Moreover, PLB phosphorylation by either protein kinase A (PKA) at Serine 16 or by Ca^{2+}-calmodulin-dependent kinase II (CaMKII) at Threonine 17 causes PLB pentamerization and dissociation from SERCA, thus removing its inhibitory effect. Using qRT-PCR and western-blot analyses, we found similar levels of SERCA2a mRNA and protein between isolated RV cardiomyocytes from control and MCT rats (Fig. 3e). In addition, no changes in total PLB protein expression were observed (Fig. 3f). However, we showed an increase in PLB phosphorylation by PKA at Serine 16, while PLB phosphorylation by CaMKII at Threonine 17 was not affected (Fig. 3f), which could account for the faster $[Ca^{2+}]_i$ transients decay time in addition to enhanced $[Ca^{2+}]_i$ transients peak amplitude.

Increased SR Ca^{2+} load in hypertrophied RV myocytes

Since the SR Ca^{2+} load is a determinant in $[Ca^{2+}]_i$ transients peak amplitude, we estimated the global SR Ca^{2+} content by rapid caffeine application (10 mM) as shown in Fig. 4a for control RV myocytes (a) and MCT-exposed RV myocytes at W1 (b), at W2 (c) and W3 (d). Caffeine-evoked $[Ca^{2+}]_i$ transients in the RV myocytes were enhanced at W3 compared to those in the control myocytes (Fig. 4b). Therefore, the increase in $[Ca^{2+}]_i$ transients amplitude at W3 may be related, at least in part, to the increase in the SR Ca^{2+} load. The caffeine-evoked $[Ca^{2+}]_i$

transients decay time was similar in myocytes from the control and MCT-exposed rats at every studied time point (Fig. 4c), suggesting preserved NCX activity. We also estimated the fractional release in electrically-evoked twitches by normalizing the $[Ca^{2+}]_i$ transients amplitude by the SR Ca^{2+} load. We showed an increase in fractional release in myocytes isolated from MCT-PH rats at W3 compared with that in control myocytes (Fig. 4d), suggesting higher RyR activity. Similarly, the capacity of the SR to accumulate Ca^{2+} at rest, as estimated by post-rest potentiation, was decreased in RV cardiomyocytes isolated from MCT-PH rats at W3 (Fig. 4e).

Increased SR Ca^{2+} leak associated with altered spatiotemporal properties of Ca^{2+} sparks in hypertrophied RV myocytes

Increased fractional release and decreased post-rest potentiation may reflect higher RyR activity during RV remodeling in PH. Opening of the RyR cluster induces a rapid, local, and brief $[Ca^{2+}]_i$ elevation called a Ca^{2+} spark. The frequency of these sparks and their properties (amplitude, duration and size) are used as markers of *in situ* RyR activity. The amount of Ca^{2+} stored in the SR is known to influence Ca^{2+} sparks' properties and activities. We hypothesized that the higher SR Ca^{2+} load measured in RV myocytes from MCT rats could contribute to alterations in Ca^{2+} spark properties. According to the fractional release and post-rest potentiation data (Fig. 4d-e), RV cardiomyocytes at W2 and W3 showed a significant increase in Ca^{2+} spark frequency compared to that in control myocytes, with a more pronounced increase at W3 (Fig. 5a-b).

To assess the biophysical characteristics of Ca^{2+} sparks, we analyzed their amplitude (measured as the peak F/F_0), full duration at half-maximum (FDHM), and full width at half-maximum (FWHM) in RV and LV myocytes from control or MCT-exposed rats. Ca^{2+} spark amplitudes were similar between RV myocytes from MCT rats (W3) and control myocytes (Fig. 5c). However, both the FDHM and FWHM were significantly increased in RV myocytes from MCT rats at W3 (Fig. 5d-e), suggesting an alteration in the intrinsic RyR cluster activity or RyR disorganization during RV remodeling in PH. Taken together, these results show increased Ca^{2+} spark frequency and a shift of the population to wider and longer Ca^{2+} sparks in RV myocytes at W3. Since Ca^{2+} spark parameters are good indicators of local SR Ca^{2+} release flux, we can conclude that the total Ca^{2+} mass (calculated by amplitude*duration*width) released through Ca^{2+} sparks was increased in RV cells (in F/F_0 ms·µm: 203.4 in 1346 MCT W3 events *vs.* 145.2 in 663 control events). Surprisingly, although $[Ca^{2+}]_i$ transients parameters were unchanged in LV myocytes from MCT rats, we observed a significant increase in the Ca^{2+} spark frequency associated with decreased Ca^{2+} spark amplitudes in LV myocytes at W3 (Fig. 5b-c).

Impairment of RyR clusters and T-tubule network integrity in hypertrophied RV myocytes

The abnormal Ca^{2+} spark activity found at W3 could be attributed to altered RyR expression and regulation by PKA-mediated phosphorylation at Ser^{2808} or by CaMKII-mediated phosphorylation at Ser^{2814}.

We estimated RyR2 expression by qRT-PCR and Western-blot. No modifications at either the mRNA level (Fig. 6a) or the protein level (Fig. 6b-c) were found in RV and LV cardiomyocytes from MCT rats compared to control cardiomyocytes.

The ratio of p-Ser^{2814}/total RyR2 was unaffected in RV and LV myocytes from MCT-PH rats at W3 (Fig. 6b-c). Surprisingly, no phosphorylation of RyR2 at Ser^{2808} (PKA-specific site) was observed in RV cells (Fig. 6d) under

basal and pathological conditions. In LV cells, the ratio of p-Ser^{2808}/total RyR2 was unchanged (Fig. 6d). Therefore, the observed modifications in RyR activity in RV cells quantified through Ca^{2+} spark analysis were not due to changes in phosphorylation. Figure 6e shows representative images of RyR2 staining by confocal microscopy in RV myocytes from control rats and rats exposed to MCT for 3 weeks. The immunolabeling against RyR2 protein further confirmed the unchanged RyR2 expression in RV cells. However, the RyR2 network appeared less organized in RV cardiomyocytes from MCT rats at W3 (Fig. 6e). Notably, this disorganization did not appear at W1 and W2 (data not shown).

T-tubule density and network integrity play pivotal roles in ECC, providing proximity between the sarcolemma and SR membrane and determining the synchrony of SR Ca^{2+} release during an action potential. Altered T-tubule morphology has been described in several hypertrophy/failure models [34] and loss of T-tubules in pathological states causes spatial dissociation between L-type Ca^{2+} channels and RyRs, leading to the formation of orphaned RyRs [35]. We next investigated potential T-tubule remodeling in MCT-PH rats. The left panel of Figure 6f shows representative T-tubule images obtained by sarcolemmal staining (Di-8-ANEPPS) using confocal microscopy at different stages during RV dysfunction progression. We found progressive T-tubule disruption with dramatic loss of T-tubule signals and loss of the regular striated pattern in RV cardiomyocytes at the advanced PH stage (W2 and W3), with milder loss in LV cells (Fig. 6f). Our findings strongly suggest that T-tubule remodeling is an important event leading to alterations in Ca^{2+} sparks and non-junctional RyRs in the right and left ventricles.

Increased expression of STIM1 Long isoform, glycosylated Orai1 and TRPC1/TRPC4 leads to enhanced I_{CRAC}-like current in hypertrophied RV myocytes

Recently, SOCE has been reported to modulate the SR Ca^{2+} content and to maintain diastolic Ca^{2+} homeostasis. Moreover, strong evidence indicates upregulated SOC expression and activity in LVH and LVF [20,23–25,27–29]. Here, we investigated whether SOC molecules could be responsible for the increased SR Ca^{2+} content in RV myocytes from MCT-PH rats.

Figure 7a shows that unglycosylated Orai1 channel expression (non-plasma membrane channels) was not significantly altered during the establishment of RV dysfunction, while glycosylated Orai1 (plasma membrane channels) expression was increased 4.5-fold 3 weeks after MCT exposure. Similar results were obtained in LV myocytes (Supplemental Fig. 3a). The classic form of the SR Ca^{2+} sensor STIM1 (90 KD) showed progressively decreased expression in RV myocytes during the development of RV dysfunction (Fig. 7a), but its expression was unchanged in LV myocytes (Supplemental Fig. 3a). Interestingly, together with reduced classic STIM1 expression at W3, Western-blot analysis revealed the emergence of the long form of STIM1, called STIM1L (Fig. 7a). No difference in STIM1L expression was observed in LV myocytes (Supplemental Fig. 3a). We next evaluated TRPCs isoform expression during RVH development. We showed that RV expression levels of TRPC1 and TRPC4 isoforms were progressively increased during RVH development (Fig. 7b). TRPC3 and TRPC6 expression levels were unchanged in RV from MCT-exposed rats (Fig. 7c), while RV TRPC5 expression was decreased 2-fold 3 weeks after PH induction (Fig. 7c). Importantly, no changes in TRPCs expression (Supplemental Fig. 3b) or in STIM2 and Orai3 expression (Supplemental Fig. 3c) were observed in LV cardiomyocytes from MCT-PH rats.

To explore whether the increases in glycosylated Orai1, STIM1L expression and TRPC1/TRPC4 expression are functional, we measured the Ca^{2+} current via patch-clamp in a whole-cell configuration under conditions in which

major protagonists controlling $[Ca^{2+}]_i$ (L-type Ca^{2+} channels, NCX) were blocked. Interestingly, in the absence of SR Ca^{2+} depletion, a standard ramp protocol elicited an almost linear current-voltage (I-V) relationship in control RV cardiomyocytes (Fig. 8a), while the I-V curve obtained in hypertrophied cardiomyocytes presented strong rectification of the inward current (Fig. 8b). Indeed, the unstimulated current densities recorded at -110 mV were strongly increased in RV myocytes from MCT-treated rats at W3 (-3.5 ± 0.3 pA/pF) compared to those in RV myocytes from control rats (-1.8 ± 0.2 pA/pF). To further characterize this inward current, we used 5 µM of BTP2, a common TRPCs/Orai channel blocker [36]. Perfusion of BTP2 significantly reduced both inward and outward currents (Fig. 8c-d). As a result, the BTP2-sensitive current was very small in control cells (-0.45 ±0 .29 and 0.06 ± 0.08 pA/pF at -110 and +50 mV). In RV myocytes isolated from MCT-PH rats at W3, the BTP2-sensitive current presented a more pronounced inward rectification compared to that in control myocytes (Fig. 8d). We recorded a significant 6-fold increase in inward and outward BTP2-sensitive currents (-2.7 ± 0.5 and 0.4 ± 0.1 pA/pF at -110 and +50 mV, respectively; *vs.* control) in hypertrophied cells compared to those in control cells (Fig. 8d). The nature of this current in non-depleted cells with potential reversal around 0 mV and strong inward rectification revealed a CRAC-like current, suggesting a mixed cation current carried by TRPCs and Orai1 channels.
In addition, the currents recorded in LV cardiomyocytes from MCT-PH rats (at W3) were unchanged compared to those in control cells (Supplemental Fig. 4). These data support the idea that the observed increase in SR Ca^{2+} content specifically in hypertrophied RV cells could be attributed to increased Ca^{2+} entry through SOCs, among other Ca^{2+} protein partners.

Pharmacological inhibition of TRPCs/Orai1 channels by BTP2 reduced the Ca^{2+} handling remodeling observed in hypertrophied RV myocytes

To further investigate the contributions of TRPCs and Orai1 to RV Ca^{2+} cycling remodeling, we analyzed electrically-evoked $[Ca^{2+}]_i$ transients, cell shortening and the SR Ca^{2+} load of isolated RV cardiomyocytes from control rats and MCT-PH rats at W3 before and after treatment with 5 µM of BTP2. In cardiomyocytes isolated from MCT rats, BTP2 (1 min of pre-incubation) application significantly reduced the amplitude of $[Ca^{2+}]_i$ transients and cell shortening (Fig. 8e). In addition, caffeine-evoked $[Ca^{2+}]_i$ transients in RV myocytes were also significantly reduced by BTP2 application (Fig. 8f). Interestingly, BTP2 administration had no impact on Ca^{2+} cycling in cardiomyocytes isolated from control rats, suggesting that SOCs did not participate in ECC in the RV at baseline. These data demonstrated that TRPCs/Orai1 channel activity, which is enhanced in MCT-PH rats, contributes to the Ca^{2+} handling remodeling involved in ECC in hypertrophied RV cardiomyocytes.

Discussion

In this study, we provided solid evidence of Ca^{2+} cycling modulation in RV myocytes, but not in LV myocytes, from rats that developed severe PH and RVH 3 weeks after MCT exposure. We showed (**i**) differences in Ca^{2+} cycling properties of the SR between RV and LV adult rat myocytes under physiological conditions; (**ii**) an increase in $[Ca^{2+}]_i$ transients amplitude associated with an increased SR Ca^{2+} load and faster Ca^{2+} reuptake leading to improved cell contraction only in RV myocytes; (**iii**) increased phosphorylation of phospholamban at Serine 16 (Ser^{16}) in RV cardiomyocytes without any changes in SERCA2a expression; (**iv**) enhanced Ca^{2+} spark activity

correlating with impaired RyR clusters and T-tubule network integrity in RV and LV cardiomyocytes; and (**v**) increases in glycosylated Orai1, TRPC1/TRPC4 expression and the STIM1L/STIM1 ratio, highlighting the roles of these molecules in RVH in the context of PH.

Echocardiography analyses demonstrated that PH induced by MCT exposure leads to progressive RVH associated with systolic dysfunction, while LV function is preserved. These data demonstrate that MCT-exposed rats developed maladaptive RVH at 3 weeks with preserved LV function and without clinical signs of heart failure (absence of mortality/sudden death, peripheral edema). Macroscopic RVH was confirmed at the cellular level by increased cell membrane capacitance associated with significant prolongation of action potential duration in isolated RV cardiomyocytes from MCT-exposed animals at W2 and W3 as well as induction of hypertrophic markers such as *ANP* and *BNP* and the switch from the adult *α-MHC* gene to the fetal *β-MHC* gene.

Under physiological conditions, the $[Ca^{2+}]_i$ transients in isolated ventricular myocytes revealed characteristic features between RV and LV myocytes, including a larger $[Ca^{2+}]_i$ transients peak and a higher SR Ca^{2+} content in LV myocytes. The difference in SR Ca^{2+} pump activity is not due to a difference in SERCA2a Ca^{2+} pump density or PLB levels, but it could be attributed to its higher catalytic activity in the LV compartment and a more inert proportion of SERCA in RV myocytes because of their stable association with PLB as previously proposed [37]. Therefore, we demonstrated a striking chamber-specific difference in intracellular Ca^{2+} cycling between healthy RVs and LVs in rats, which is consistent with physiological differences in afterload and hemodynamic load between the RV and LV chambers.

After the pathological insult induced by monocrotaline, the RV developed hypertrophy, which was statistically evident from 2 weeks after exposure. Concomitantly, the action potential duration was increased at W2 and W3. Recently, we demonstrated that KCNK3 channel loss of function and a decrease in Kv4.2, Kv4.3 and Kv1.5 expression, resulting in decreased I_{KCNK3} current, outward sustained potassium current (I_{sus}) and transient outward potassium current (I_{to}) contribute to APD prolongation in RV cardiomyocytes [33].

In addition, action potential prolongation is a hallmark of hypertrophy in the LV and enhances Ca^{2+} entry, producing higher $[Ca^{2+}]_i$ transients even with maintained L-type Ca^{2+} channel expression and function [17,38]. At W3, in addition to action potential prolongation, the enhanced $[Ca^{2+}]_i$ transients may also be due to an increase in the SR Ca^{2+} load. Consistent with the preserved *in vivo* LV function, no modification in Ca^{2+} cycling was observed in LV myocytes.

PLB regulates SERCA pumps by reducing their Ca^{2+} affinity. This mechanism is a dynamic process that depends on $[Ca^{2+}]_i$, phosphorylation and homo-oligomeric states. Altered levels of SERCA2a and PLB have been found in MCT-treated rats at the severe heart failure stage [39,40]. In contrast, no changes have been demonstrated in SERCA and PLB levels in mild chronic PH [16]. Although we found no changes in SERCA2a and PLB protein abundance, we demonstrated increased PLB phosphorylation by PKA at Ser^{16}, which could account for the higher SR Ca^{2+} content.

In addition, we showed an increase in Ca^{2+} spark frequency and a shift of the population to wider and longer Ca^{2+} sparks in hypertrophied RV myocytes after 3 weeks of MCT exposure. These modifications were not due to changes in protein expression or phosphorylation, suggesting an alteration in dyads structure. Indeed, by immunostaining, we reported robust disorganization of the RyR2 network in RV cardiomyocytes from MCT rats at W3, suggesting an altered junctional SR structure.

Moreover, the T-tubule network was disrupted as in other models of PH-induced heart failure [34,41,42]. This disruption could produce Ca^{2+} sparks whose diffusion is not restricted in the space by the adjacent T-tubules, thus accounting for the wider and longer Ca^{2+} sparks that we observed.

Here, we found progressive T-tubule network disruption and disorganization with dramatic loss of the regular striated pattern at the advanced PH stage (W2 and W3) in RV and LV cardiomyocytes, which could be an important factor leading to the emergence of non-junctional RyRs. In the LV compartment, the altered T-tubule network could also be due the deviated interventricular septum curve observed at W3 (data not shown).

TRPCs, STIM1 and Orai1 molecules were identified as key participants in SOCE in almost all non-excitable cells [18,19,43,44], which has been described as a key feature in replenishing intracellular Ca^{2+} stores. While the functional role of TRPCs/Orai1/STIM1-mediated SOCE in non-excitable cells has been clearly characterized, its cardiac physiological role is less clear. TRPCs or STIM1 has been reported to colocalize with key regulators of ECC such as SERCA, NCX, PLB and RyRs in neonatal and adult rat hearts [45–51], regulating the amount of Ca^{2+} in the SR. We and others suggested that TRPCs/Orai1/STIM1-mediated SOCE plays a role in the regulating cardiac diastolic Ca^{2+} homeostasis [20–23,25,26,29] through a SGK1-dependent mechanism[20].

In the context of cardiac diseases, *in vitro and in vivo* data clearly demonstrate that TRPCs-, STIM1/Orai1- and Orai3-dependent Ca^{2+} entry are instrumental for pathological LVH development [20, 23, 25, 26, 29, 45, 49, 52–60]. In this study, we speculated that, in collaboration with SERCA2a/PLB activity, SOCE could contribute to the observed increase in the SR Ca^{2+} load in experimental RVH induced by MCT exposure. Surprisingly, we showed that STIM1 expression is progressively and significantly reduced in hypertrophied RV cardiomyocytes from MCT-exposed animals. However, induction of STIM1L, TRPC1 and TRPC4 expression was observed under pathological conditions. These modifications were not detected in LV cardiomyocytes. In addition, we found a marked increase in the glycosylated Orai1 form in both ventricles. The changes in SOC machinery expression were correlated with an increased BTP2-sensitive current only in non-depleted RV cells, with a predominantly inward rectifying current reflecting Orai1-dependent I_{CRAC}-like currents. The outward current and the reversal potential suggest that non-selective cationic channels, such as TRPCs channels, could contribute to this current together with Orai1. Similarly, we previously reported an I_{SOC} in neonatal cardiomyocytes carried by a dynamic assembly of TRPC-STIM1-Orai1 [20]. Similar to our findings, Hulot et al. also found an inward rectifying current in adult LV myocytes that is rapidly and fully active even when Ca^{2+} stores are repleted, reflecting more rapid kinetics of I_{SOC} activation in cardiac myocytes compared to those of non-excitable cells [23]. This faster activation and store-independent current may be explained, at least in part, by the constitutive association of STIM1 and Orai1/TRPCs at the membrane as previously observed in sinoatrial node cells [61] or by the pre-constituted 'punctate' form of STIM1 without the need for Ca^{2+} store depletion in neonatal and adult cardiomyocytes [53]. Furthermore, in skeletal muscle, STIM1L has been demonstrated to interact with actin to form permanent clusters and to activate Orai1 and TRPC1/4 channels, allowing immediate SOCE activation[62,63].

Moreover, inhibition of SOCs prevented the Ca^{2+} cycling modulation observed in cardiomyocytes from MCT rats. Therefore, we revealed for the first time that the Ca^{2+} current elicited by STIM1L and TRPCs/Orai1 contributes to the enhanced SR Ca^{2+} content in RV hypertrophied cardiomyocytes. Interestingly, inositol 1,4,5-Trisphosphate Receptors (IP_3R) have been considered as other regulators of cardiac ECC [64,65]. Indeed, in LV cardiomyocytes, Ca^{2+} mobilized from the SR via IP_3R2 contributed to decreased resting membrane potentials, prolonged action potentials, and the occurrence of early afterdepolarizations [65]. Interestingly, we found that the IP_3R2 isoform

was strongly increased in RV compartments 3 weeks after PH induction (Supplemental Figure 5). Further investigations were required to determine whether IP_3R2 in association with SOCs could contribute to Ca^{2+} homeostasis remodeling in RV cardiomyocytes from PH rats.

A discrepancy was observed between the results obtained from isolated cells (higher $[Ca^{2+}]_i$ transients amplitude, higher SR Ca^{2+} load and improved cell contractility) and the loss of *in vivo* RV function measured by echocardiography (by reduced RV fractional shortening). First, capillary rarefaction can partly explain the loss of RV function in MCT-PH rats. Indeed, capillary rarefaction has been reported in the RV compartment of PAH patients [66,67] and in an experimental model of PH [3,67]. Importantly, improved RV microvessels density by pharmacological miR-126 upregulation improved RV function in experimental PAH, confirming that capillary density is crucial for RV cardiac function [67]. Here, we confirmed the loss of capillary density in the RV compartment of MCT-PH rats. Moreover, RV fibroblasts and extracellular matrix production characterized by significantly increased expression of collagen isoforms [3,36] play important roles in the pathogenesis of RVH and RV dysfunction [68,69]. In patients with severe aortic valve stenosis, the extent of myocardial fibrosis has a significant effect on clinical status and long-term survival [37]. In addition, myocardial fibrosis contributes to sudden cardiac death, ventricular tachyarrhythmias, LV dysfunction, and heart failure in hypertrophic cardiomyopathy [38]. We confirmed a severe increase in RV fibrosis in MCT-PH rats as previously observed [38,70]. Endothelin-1 (ET-1) is known to activate cardiac fibroblasts and to promote the synthesis of matrix proteins [71,72]. We found overexpression of endothelin receptors (ET-1RA and ET-1RB) in the RV of MCT rats (Supplemental Figure 5). In addition, increased wall stress and hypoxia are stimuli that promote ET-1 release [73,74]. According to these results, increased ET-1 signaling could contribute to RV fibrosis and inflammation associated with RV dysfunction.

Moreover, inflammation played a dual role in the development of both pulmonary vascular remodeling and RV failure [75]. Abnormal cytokine expression was shown to impair myocardial contractility and cardiac function [76] through multiple mechanisms [75] . We showed that RV inflammation was abnormally increased in MCT-PH rats, contributing to the establishment of RV dysfunction. Taken together, the alteration in Ca^{2+} handling in cardiac myocytes, which increases cell contractile function, tends to compensate the loss of function by tissue fibrosis and decrease in capillary density.

In conclusion, despite intense characterization of the *in vivo* cardiac dysfunction in MCT-induced PH, the functional demonstration of Ca^{2+} deregulation in this model is not unequivocally established in RV and LV cardiomyocytes. Altogether, these data strongly support an enhanced Ca^{2+} current elicited by STIM1L and TRPCs/Orai1 that contributes to the enhanced SR Ca^{2+} content together with higher SERCA activity in hypertrophied RV cardiomyocytes.

Acknowledgments This work was supported by research grants from INSERM, National Funding Agency for Research (ANR) (Grant ANR-13-JSV1-0011-01, ANR-13-BSV1-0023 and ANR-15-CE14–0005), Laboratoire d'Excellence (LabEx) en Recherche sur le Médicament et l'Innovation Thérapeutique (LERMIT), Legs Poix (Chancellerie des Universités de Paris) and by the French patient association HTAP France. We thank Katell Bon-Mardion for her excellent technical assistance. We thank the AnimEX platform from the University of Paris-Sud for animal care. F.A. is supported by a grant from Aviesan and by Lefoulon Delalande Institute.

Conflict of interest M.H. has relationships with drug companies including Actelion, Bayer, GSK, Novartis, and Pfizer. The other authors report no conflicts.

References

[1] N. Galiè, M. Humbert, J.-L. Vachiery, S. Gibbs, I. Lang, A. Torbicki, G. Simonneau, A. Peacock, A. Vonk Noordegraaf, M. Beghetti, A. Ghofrani, M.A. Gomez Sanchez, G. Hansmann, W. Klepetko, P. Lancellotti, M. Matucci, T. McDonagh, L.A. Pierard, P.T. Trindade, M. Zompatori, M. Hoeper, V. Aboyans, A. Vaz Carneiro, S. Achenbach, S. Agewall, Y. Allanore, R. Asteggiano, L. Paolo Badano, J. Albert Barberà, H. Bouvaist, H. Bueno, R.A. Byrne, S. Carerj, G. Castro, Ç. Erol, V. Falk, C. Funck-Brentano, M. Gorenflo, J. Granton, B. Iung, D.G. Kiely, P. Kirchhof, B. Kjellstrom, U. Landmesser, J. Lekakis, C. Lionis, G.Y.H. Lip, S.E. Orfanos, M.H. Park, M.F. Piepoli, P. Ponikowski, M.-P. Revel, D. Rigau, S. Rosenkranz, H. Völler, J. Luis Zamorano, 2015 ESC/ERS Guidelines for the diagnosis and treatment of pulmonary hypertension: The Joint Task Force for the Diagnosis and Treatment of Pulmonary Hypertension of the European Society of Cardiology (ESC) and the European Respiratory Society (ERS): Endorsed by: Association for European Paediatric and Congenital Cardiology (AEPC), International Society for Heart and Lung Transplantation (ISHLT), Eur. Heart J. 37 (2016) 67–119. doi:10.1093/eurheartj/ehv317.

[2] M. Humbert, E.M.T. Lau, D. Montani, X. Jaïs, O. Sitbon, G. Simonneau, Advances in therapeutic interventions for patients with pulmonary arterial hypertension, Circulation. 130 (2014) 2189–2208. doi:10.1161/CIRCULATIONAHA.114.006974.

[3] H.J. Bogaard, K. Abe, A. Vonk Noordegraaf, N.F. Voelkel, The right ventricle under pressure: cellular and molecular mechanisms of right-heart failure in pulmonary hypertension, Chest. 135 (2009) 794–804. doi:10.1378/chest.08-0492.

[4] F. Haddad, S.A. Hunt, D.N. Rosenthal, D.J. Murphy, Right ventricular function in cardiovascular disease, part I: Anatomy, physiology, aging, and functional assessment of the right ventricle, Circulation. 117 (2008) 1436–1448. doi:10.1161/CIRCULATIONAHA.107.653576.

[5] S. Zaffran, R.G. Kelly, S.M. Meilhac, M.E. Buckingham, N.A. Brown, Right ventricular myocardium derives from the anterior heart field, Circ. Res. 95 (2004) 261–268. doi:10.1161/01.RES.0000136815.73623.BE.

[6] A.T. Roe, M. Frisk, W.E. Louch, Targeting cardiomyocyte Ca2+ homeostasis in heart failure, Curr. Pharm. Des. 21 (2015) 431–448.

[7] J.J. Mercadier, A.M. Lompré, P. Duc, K.R. Boheler, J.B. Fraysse, C. Wisnewsky, P.D. Allen, M. Komajda, K. Schwartz, Altered sarcoplasmic reticulum Ca2(+)-ATPase gene expression in the human ventricle during end-stage heart failure, J. Clin. Invest. 85 (1990) 305–309. doi:10.1172/JCI114429.

[8] S.O. Marx, S. Reiken, Y. Hisamatsu, T. Jayaraman, D. Burkhoff, N. Rosemblit, A.R. Marks, PKA phosphorylation dissociates FKBP12.6 from the calcium release channel (ryanodine receptor): defective regulation in failing hearts, Cell. 101 (2000) 365–376.

[9] A.M. Gómez, B. Schwaller, H. Porzig, G. Vassort, E. Niggli, M. Egger, Increased exchange current but normal Ca2+ transport via Na+-Ca2+ exchange during cardiac hypertrophy after myocardial infarction, Circ. Res. 91 (2002) 323–330.

[10] A.M. Gómez, H.H. Valdivia, H. Cheng, M.R. Lederer, L.F. Santana, M.B. Cannell, S.A. McCune, R.A. Altschuld, W.J. Lederer, Defective excitation-contraction coupling in experimental cardiac hypertrophy and heart failure, Science. 276 (1997) 800–806.

[11] E. Wagner, M.A. Lauterbach, T. Kohl, V. Westphal, G.S.B. Williams, J.H. Steinbrecher, J.-H. Streich, B. Korff, H.-T.M. Tuan, B. Hagen, S. Luther, G. Hasenfuss, U. Parlitz, M.S. Jafri, S.W. Hell, W.J. Lederer, S.E. Lehnart, Stimulated emission depletion live-cell super-resolution imaging shows proliferative remodeling of T-tubule membrane structures after myocardial infarction, Circ. Res. 111 (2012) 402–414. doi:10.1161/CIRCRESAHA.112.274530.

[12] J.J. Ryan, G. Marsboom, S.L. Archer, Rodent models of group 1 pulmonary hypertension, Handb Exp Pharmacol. 218 (2013) 105–149. doi:10.1007/978-3-642-38664-0_5.

[13] F. Brunner, G. Wölkart, S. Haleen, Defective intracellular calcium handling in monocrotaline-induced right ventricular hypertrophy: protective effect of long-term endothelin-A receptor blockade with 2-benzo[1,3]dioxol-5-yl-3-benzyl-4-(4-methoxy-phenyl-)- 4-oxobut-2-enoate-sodium (PD 155080), J. Pharmacol. Exp. Ther. 300 (2002) 442–449.

[14] G. Wölkart, H. Strömer, F. Brunner, Calcium handling and role of endothelin-1 in monocrotaline right ventricular hypertrophy of the rat, J. Mol. Cell. Cardiol. 32 (2000) 1995–2005. doi:10.1006/jmcc.2000.1231.

[15] T. Kuramochi, M. Honda, K. Tanaka, K. Enomoto, M. Hashimoto, S. Morioka, Calcium transients in single myocytes and membranous ultrastructures during the development of cardiac hypertrophy and heart failure in rats, Clin. Exp. Pharmacol. Physiol. 21 (1994) 1009–1018.

[16] Y.-P. Xie, B. Chen, P. Sanders, A. Guo, Y. Li, K. Zimmerman, L.-C. Wang, R.M. Weiss, I.M. Grumbach, M.E. Anderson, L.-S. Song, Sildenafil prevents and reverses transverse-tubule remodeling and Ca(2+) handling dysfunction in right ventricle failure induced by pulmonary artery hypertension, Hypertension. 59 (2012) 355–362. doi:10.1161/HYPERTENSIONAHA.111.180968.

[17] D. Benoist, R. Stones, M.J. Drinkhill, A.P. Benson, Z. Yang, C. Cassan, S.H. Gilbert, D.A. Saint, O. Cazorla, D.S. Steele, O. Bernus, E. White, Cardiac arrhythmia mechanisms in rats with heart failure induced by pulmonary hypertension, Am. J. Physiol. Heart Circ. Physiol. 302 (2012) H2381-2395. doi:10.1152/ajpheart.01084.2011.
[18] I.S. Ambudkar, L.B. de Souza, H.L. Ong, TRPC1, Orai1, and STIM1 in SOCE: Friends in tight spaces, Cell Calcium. 63 (2017) 33–39. doi:10.1016/j.ceca.2016.12.009.
[19] S. Choi, J. Maleth, A. Jha, K.P. Lee, M.S. Kim, I. So, M. Ahuja, S. Muallem, The TRPCs-STIM1-Orai interaction, Handb Exp Pharmacol. 223 (2014) 1035–1054. doi:10.1007/978-3-319-05161-1_13.
[20] J. Sabourin, F. Bartoli, F. Antigny, A.M. Gomez, J.-P. Benitah, Transient Receptor Potential Canonical (TRPC)/Orai1-dependent Store-operated Ca2+ Channels: NEW TARGETS OF ALDOSTERONE IN CARDIOMYOCYTES, J. Biol. Chem. 291 (2016) 13394–13409. doi:10.1074/jbc.M115.693911.
[21] C.D. Touchberry, C.J. Elmore, T.M. Nguyen, J.J. Andresen, X. Zhao, M. Orange, N. Weisleder, M. Brotto, W.C. Claycomb, M.J. Wacker, Store-operated calcium entry is present in HL-1 cardiomyocytes and contributes to resting calcium, Biochem. Biophys. Res. Commun. 416 (2011) 45–50. doi:10.1016/j.bbrc.2011.10.133.
[22] M. Voelkers, M. Salz, N. Herzog, D. Frank, N. Dolatabadi, N. Frey, N. Gude, O. Friedrich, W.J. Koch, H.A. Katus, M.A. Sussman, P. Most, Orai1 and Stim1 regulate normal and hypertrophic growth in cardiomyocytes, J. Mol. Cell. Cardiol. 48 (2010) 1329–1334. doi:10.1016/j.yjmcc.2010.01.020.
[23] J.-S. Hulot, J. Fauconnier, D. Ramanujam, A. Chaanine, F. Aubart, Y. Sassi, S. Merkle, O. Cazorla, A. Ouillé, M. Dupuis, L. Hadri, D. Jeong, S. Mühlstedt, J. Schmitt, A. Braun, L. Bénard, Y. Saliba, B. Laggerbauer, B. Nieswandt, A. Lacampagne, R.J. Hajjar, A.-M. Lompré, S. Engelhardt, Critical role for stromal interaction molecule 1 in cardiac hypertrophy, Circulation. 124 (2011) 796–805. doi:10.1161/CIRCULATIONAHA.111.031229.
[24] X. Luo, B. Hojayev, N. Jiang, Z.V. Wang, S. Tandan, A. Rakalin, B.A. Rothermel, T.G. Gillette, J.A. Hill, STIM1-dependent store-operated Ca^{2+} entry is required for pathological cardiac hypertrophy, J. Mol. Cell. Cardiol. 52 (2012) 136–147. doi:10.1016/j.yjmcc.2011.11.003.
[25] T. Ohba, H. Watanabe, M. Murakami, Y. Takahashi, K. Iino, S. Kuromitsu, Y. Mori, K. Ono, T. Iijima, H. Ito, Upregulation of TRPC1 in the development of cardiac hypertrophy, J. Mol. Cell. Cardiol. 42 (2007) 498–507. doi:10.1016/j.yjmcc.2006.10.020.
[26] Y. Saliba, M. Keck, A. Marchand, F. Atassi, A. Ouillé, O. Cazorla, M. Trebak, C. Pavoine, A. Lacampagne, J.-S. Hulot, N. Farès, J. Fauconnier, A.-M. Lompré, Emergence of Orai3 activity during cardiac hypertrophy, Cardiovasc. Res. 105 (2015) 248–259. doi:10.1093/cvr/cvu207.
[27] S. Satoh, H. Tanaka, Y. Ueda, J.-I. Oyama, M. Sugano, H. Sumimoto, Y. Mori, N. Makino, Transient receptor potential (TRP) protein 7 acts as a G protein-activated Ca2+ channel mediating angiotensin II-induced myocardial apoptosis, Mol. Cell. Biochem. 294 (2007) 205–215. doi:10.1007/s11010-006-9261-0.
[28] M. Völkers, N. Dolatabadi, N. Gude, P. Most, M.A. Sussman, D. Hassel, Orai1 deficiency leads to heart failure and skeletal myopathy in zebrafish, J. Cell. Sci. 125 (2012) 287–294. doi:10.1242/jcs.090464.
[29] X. Wu, P. Eder, B. Chang, J.D. Molkentin, TRPC channels are necessary mediators of pathologic cardiac hypertrophy, Proc. Natl. Acad. Sci. U.S.A. 107 (2010) 7000–7005. doi:10.1073/pnas.1001825107.
[30] R. Zhou, P. Hang, W. Zhu, Z. Su, H. Liang, Z. Du, Whole genome network analysis of ion channels and connexins in myocardial infarction, Cell. Physiol. Biochem. 27 (2011) 299–304. doi:10.1159/000327956.
[31] A. Houssaini, S. Abid, N. Mouraret, F. Wan, D. Rideau, M. Saker, E. Marcos, C.-M. Tissot, J.-L. Dubois-Randé, V. Amsellem, S. Adnot, Rapamycin reverses pulmonary artery smooth muscle cell proliferation in pulmonary hypertension, Am. J. Respir. Cell Mol. Biol. 48 (2013) 568–577. doi:10.1165/rcmb.2012-0429OC.
[32] F. Antigny, A. Hautefort, J. Meloche, M. Belacel-Ouari, B. Manoury, C. Rucker-Martin, C. Péchoux, F. Potus, V. Nadeau, E. Tremblay, G. Ruffenach, A. Bourgeois, P. Dorfmüller, S. Breuils-Bonnet, E. Fadel, B. Ranchoux, P. Jourdon, B. Girerd, D. Montani, S. Provencher, S. Bonnet, G. Simonneau, M. Humbert, F. Perros, Potassium Channel Subfamily K Member 3 (KCNK3) Contributes to the Development of Pulmonary Arterial Hypertension, Circulation. 133 (2016) 1371–1385. doi:10.1161/CIRCULATIONAHA.115.020951.
[33] W.E. Louch, O.M. Sejersted, F. Swift, There goes the neighborhood: pathological alterations in T-tubule morphology and consequences for cardiomyocyte Ca2+ handling, J. Biomed. Biotechnol. 2010 (2010) 503906. doi:10.1155/2010/503906.
[34] L.-S. Song, E.A. Sobie, S. McCulle, W.J. Lederer, C.W. Balke, H. Cheng, Orphaned ryanodine receptors in the failing heart, Proc. Natl. Acad. Sci. U.S.A. 103 (2006) 4305–4310. doi:10.1073/pnas.0509324103.
[35] J.W. Putney, Pharmacology of store-operated calcium channels, Mol. Interv. 10 (2010) 209–218. doi:10.1124/mi.10.4.4.
[36] V. Sathish, A. Xu, M. Karmazyn, S.M. Sims, N. Narayanan, Mechanistic basis of differences in Ca2+ -handling properties of sarcoplasmic reticulum in right and left ventricles of normal rat myocardium, Am. J. Physiol. Heart Circ. Physiol. 291 (2006) H88-96. doi:10.1152/ajpheart.01372.2005.

[37] M. Lambert, A. Boet, C. Rucker-Martin, P. Mendes-Ferreira, V. Capuano, S. Hatem, R. Adão, C. Brás-Silva, A. Hautefort, J.-B. Michel, P. Dorfmuller, E. Fadel, T. Kotsimbos, L. Price, P. Jourdon, D. Montani, M. Humbert, F. Perros, F. Antigny, Loss of KCNK3 is a hallmark of RV hypertrophy/dysfunction associated with pulmonary hypertension, Cardiovasc. Res. (2018). doi:10.1093/cvr/cvy016.

[38] M. Rocchetti, L. Sala, R. Rizzetto, L.I. Staszewsky, M. Alemanni, V. Zambelli, I. Russo, L. Barile, L. Cornaghi, C. Altomare, C. Ronchi, G. Mostacciuolo, J. Lucchetti, M. Gobbi, R. Latini, A. Zaza, Ranolazine prevents INaL enhancement and blunts myocardial remodelling in a model of pulmonary hypertension, Cardiovasc. Res. 104 (2014) 37–48. doi:10.1093/cvr/cvu188.

[39] L. Hadri, R.G. Kratlian, L. Benard, B.A. Maron, P. Dorfmüller, D. Ladage, C. Guignabert, K. Ishikawa, J. Aguero, B. Ibanez, I.C. Turnbull, E. Kohlbrenner, L. Liang, K. Zsebo, M. Humbert, J.-S. Hulot, Y. Kawase, R.J. Hajjar, J.A. Leopold, Therapeutic efficacy of AAV1.SERCA2a in monocrotaline-induced pulmonary arterial hypertension, Circulation. 128 (2013) 512–523. doi:10.1161/CIRCULATIONAHA.113.001585.

[40] H. Kögler, O. Hartmann, K. Leineweber, P. Nguyen van, P. Schott, O.-E. Brodde, G. Hasenfuss, Mechanical load-dependent regulation of gene expression in monocrotaline-induced right ventricular hypertrophy in the rat, Circ. Res. 93 (2003) 230–237. doi:10.1161/01.RES.0000085042.89656.C7.

[41] A. Guo, C. Zhang, S. Wei, B. Chen, L.-S. Song, Emerging mechanisms of T-tubule remodelling in heart failure, Cardiovasc. Res. 98 (2013) 204–215. doi:10.1093/cvr/cvt020.

[42] L. Sallé, F. Brette, T-tubules: a key structure of cardiac function and dysfunction, Arch Mal Coeur Vaiss. 100 (2007) 225–230.

[43] F. Antigny, H. Jousset, S. König, M. Frieden, Thapsigargin activates Ca^{2+} entry both by store-dependent, STIM1/Orai1-mediated, and store-independent, TRPC3/PLC/PKC-mediated pathways in human endothelial cells, Cell Calcium. 49 (2011) 115–127. doi:10.1016/j.ceca.2010.12.001.

[44] H.L. Ong, L.B. de Souza, I.S. Ambudkar, Role of TRPC Channels in Store-Operated Calcium Entry, Adv. Exp. Med. Biol. 898 (2016) 87–109. doi:10.1007/978-3-319-26974-0_5.

[45] R.N. Correll, S.A. Goonasekera, J.H. van Berlo, A.R. Burr, F. Accornero, H. Zhang, C.A. Makarewich, A.J. York, M.A. Sargent, X. Chen, S.R. Houser, J.D. Molkentin, STIM1 elevation in the heart results in aberrant Ca^{2+} handling and cardiomyopathy, J. Mol. Cell. Cardiol. 87 (2015) 38–47. doi:10.1016/j.yjmcc.2015.07.032.

[46] G. Zhao, T. Li, D.X.P. Brochet, P.B. Rosenberg, W.J. Lederer, STIM1 enhances SR Ca2+ content through binding phospholamban in rat ventricular myocytes, Proc. Natl. Acad. Sci. U.S.A. 112 (2015) E4792-4801. doi:10.1073/pnas.1423295112.

[47] X. Zhu-Mauldin, S.A. Marsh, L. Zou, R.B. Marchase, J.C. Chatham, Modification of STIM1 by O-linked N-acetylglucosamine (O-GlcNAc) attenuates store-operated calcium entry in neonatal cardiomyocytes, J. Biol. Chem. 287 (2012) 39094–39106. doi:10.1074/jbc.M112.383778.

[48] B. Doleschal, U. Primessnig, G. Wölkart, S. Wolf, M. Schernthaner, M. Lichtenegger, T.N. Glasnov, C.O. Kappe, B. Mayer, G. Antoons, F. Heinzel, M. Poteser, K. Groschner, TRPC3 contributes to regulation of cardiac contractility and arrhythmogenesis by dynamic interaction with NCX1, Cardiovasc. Res. 106 (2015) 163–173. doi:10.1093/cvr/cvv022.

[49] F. Bartoli, J. Sabourin, Cardiac Remodeling and Disease: Current Understanding of STIM1/Orai1-Mediated Store-Operated Ca2+Entry in Cardiac Function and Pathology, Adv. Exp. Med. Biol. 993 (2017) 523–534. doi:10.1007/978-3-319-57732-6_26.

[50] M. Goel, C.-D. Zuo, W.G. Sinkins, W.P. Schilling, TRPC3 channels colocalize with Na+/Ca2+ exchanger and Na+ pump in axial component of transverse-axial tubular system of rat ventricle, Am. J. Physiol. Heart Circ. Physiol. 292 (2007) H874-883. doi:10.1152/ajpheart.00785.2006.

[51] Ca(2+) influx through L-type Ca(2+) channels and transient receptor potential channels activates pathological hypertrophy signaling. - PubMed - NCBI, (n.d.). https://www-ncbi-nlm-nih-gov.gate2.inist.fr/pubmed/?term=22921230 (accessed February 15, 2018).

[52] L. Bénard, J.G. Oh, M. Cacheux, A. Lee, M. Nonnenmacher, D.S. Matasic, E. Kohlbrenner, C. Kho, C. Pavoine, R.J. Hajjar, J.-S. Hulot, Cardiac Stim1 Silencing Impairs Adaptive Hypertrophy and Promotes Heart Failure Through Inactivation of mTORC2/Akt Signaling, Circulation. 133 (2016) 1458–1471; discussion 1471. doi:10.1161/CIRCULATIONAHA.115.020678.

[53] C. Parks, M.A. Alam, R. Sullivan, S. Mancarella, STIM1-dependent Ca(2+) microdomains are required for myofilament remodeling and signaling in the heart, Sci Rep. 6 (2016) 25372. doi:10.1038/srep25372.

[54] C.D. Troupes, M. Wallner, G. Borghetti, C. Zhang, S. Mohsin, D. von Lewinski, R.M. Berretta, H. Kubo, X. Chen, J. Soboloff, S.R. Houser, Role of STIM1 in Hypertrophy-Related Contractile Dysfunction, Circ. Res. (2017). doi:10.1161/CIRCRESAHA.117.311094.

[55] M. Freichel, M. Berlin, A. Schürger, I. Mathar, L. Bacmeister, R. Medert, W. Frede, A. Marx, S. Segin, J.E.C. Londoño, TRP Channels in the Heart, in: T.L.R. Emir (Ed.), Neurobiology of TRP Channels, 2nd ed., CRC Press/Taylor & Francis, Boca Raton (FL), 2017. http://www.ncbi.nlm.nih.gov/books/NBK476106/ (accessed February 13, 2018).

[56] P. Eder, Cardiac Remodeling and Disease: SOCE and TRPC Signaling in Cardiac Pathology, Adv. Exp. Med. Biol. 993 (2017) 505–521. doi:10.1007/978-3-319-57732-6_25.
[57] M. Seth, Z.-S. Zhang, L. Mao, V. Graham, J. Burch, J. Stiber, L. Tsiokas, M. Winn, J. Abramowitz, H.A. Rockman, L. Birnbaumer, P. Rosenberg, TRPC1 channels are critical for hypertrophic signaling in the heart, Circ. Res. 105 (2009) 1023–1030. doi:10.1161/CIRCRESAHA.109.206581.
[58] H. Watanabe, M. Murakami, T. Ohba, K. Ono, H. Ito, The pathological role of transient receptor potential channels in heart disease, Circ. J. 73 (2009) 419–427.
[59] TRPC6 fulfills a calcineurin signaling circuit during pathologic cardiac remodeling. - PubMed - NCBI, (n.d.). https://www-ncbi-nlm-nih-gov.gate2.inist.fr/pubmed/17099778 (accessed February 13, 2018).
[60] TRPC3 and TRPC6 are essential for angiotensin II-induced cardiac hypertrophy. - PubMed - NCBI, (n.d.). https://www-ncbi-nlm-nih-gov.gate2.inist.fr/pubmed/17082763 (accessed February 13, 2018).
[61] H. Zhang, A.Y. Sun, J.J. Kim, V. Graham, E.A. Finch, I. Nepliouev, G. Zhao, T. Li, W.J. Lederer, J.A. Stiber, G.S. Pitt, N. Bursac, P.B. Rosenberg, STIM1-Ca2+ signaling modulates automaticity of the mouse sinoatrial node, Proc. Natl. Acad. Sci. U.S.A. 112 (2015) E5618-5627. doi:10.1073/pnas.1503847112.
[62] F. Antigny, J. Sabourin, S. Saüc, L. Bernheim, S. Koenig, M. Frieden, TRPC1 and TRPC4 channels functionally interact with STIM1L to promote myogenesis and maintain fast repetitive Ca(2+) release in human myotubes, Biochim. Biophys. Acta. 1864 (2017) 806–813. doi:10.1016/j.bbamcr.2017.02.003.
[63] B. Darbellay, S. Arnaudeau, C.R. Bader, S. Konig, L. Bernheim, STIM1L is a new actin-binding splice variant involved in fast repetitive Ca2+ release, J. Cell Biol. 194 (2011) 335–346. doi:10.1083/jcb.201012157.
[64] H.L. Roderick, B.C. Knollmann, Inositol 1,4,5-trisphosphate receptors: “exciting” players in cardiac excitation-contraction coupling?, Circulation. 128 (2013) 1273–1275. doi:10.1161/CIRCULATIONAHA.113.005157.
[65] Inositol 1, 4, 5-trisphosphate receptors and human left ventricular myocytes. - PubMed - NCBI, (n.d.). https://www-ncbi-nlm-nih-gov.gate2.inist.fr/pubmed/23983250 (accessed February 13, 2018).
[66] L. Piao, Y.-H. Fang, K. Parikh, J.J. Ryan, P.T. Toth, S.L. Archer, Cardiac glutaminolysis: a maladaptive cancer metabolism pathway in the right ventricle in pulmonary hypertension, J. Mol. Med. 91 (2013) 1185–1197. doi:10.1007/s00109-013-1064-7.
[67] F. Potus, G. Ruffenach, A. Dahou, C. Thebault, S. Breuils-Bonnet, È. Tremblay, V. Nadeau, R. Paradis, C. Graydon, R. Wong, I. Johnson, R. Paulin, A.C. Lajoie, J. Perron, E. Charbonneau, P. Joubert, P. Pibarot, E.D. Michelakis, S. Provencher, S. Bonnet, Downregulation of MicroRNA-126 Contributes to the Failing Right Ventricle in Pulmonary Arterial Hypertension, Circulation. 132 (2015) 932–943. doi:10.1161/CIRCULATIONAHA.115.016382.
[68] N.G. Frangogiannis, Fibroblasts and the extracellular matrix in right ventricular disease, Cardiovasc. Res. 113 (2017) 1453–1464. doi:10.1093/cvr/cvx146.
[69] B. Egemnazarov, S. Crnkovic, B.M. Nagy, H. Olschewski, G. Kwapiszewska, Right ventricular fibrosis and dysfunction: Actual concepts and common misconceptions, Matrix Biol. (2018). doi:10.1016/j.matbio.2018.01.010.
[70] A.P. Lourenço, R. Roncon-Albuquerque, C. Brás-Silva, B. Faria, J. Wieland, T. Henriques-Coelho, J. Correia-Pinto, A.F. Leite-Moreira, Myocardial dysfunction and neurohumoral activation without remodeling in left ventricle of monocrotaline-induced pulmonary hypertensive rats, Am. J. Physiol. Heart Circ. Physiol. 291 (2006) H1587-1594. doi:10.1152/ajpheart.01004.2005.
[71] E.A. Nielsen, M. Sun, O. Honjo, V.E. Hjortdal, A.N. Redington, M.K. Friedberg, Dual Endothelin Receptor Blockade Abrogates Right Ventricular Remodeling and Biventricular Fibrosis in Isolated Elevated Right Ventricular Afterload, PLoS ONE. 11 (2016) e0146767. doi:10.1371/journal.pone.0146767.
[72] K.T.B. Mouchaers, I. Schalij, A.M.G. Versteilen, A.M. Hadi, G.P. van Nieuw Amerongen, V.W.M. van Hinsbergh, P.E. Postmus, W.J. van der Laarse, A. Vonk-Noordegraaf, Endothelin receptor blockade combined with phosphodiesterase-5 inhibition increases right ventricular mitochondrial capacity in pulmonary arterial hypertension, Am. J. Physiol. Heart Circ. Physiol. 297 (2009) H200-207. doi:10.1152/ajpheart.00893.2008.
[73] C.S. Moravec, E.E. Reynolds, R.W. Stewart, M. Bond, Endothelin is a positive inotropic agent in human and rat heart in vitro, Biochem. Biophys. Res. Commun. 159 (1989) 14–18.
[74] S. Dhein, C. Giessler, T. Wangemann, R.E. Silber, H.R. Zerkowski, O.E. Brodde, Differential pattern of endothelin-1-induced inotropic effects in right atria and left ventricles of the human heart, J. Cardiovasc. Pharmacol. 36 (2000) 564–569.
[75] X.-Q. Sun, A. Abbate, H.-J. Bogaard, Role of cardiac inflammation in right ventricular failure, Cardiovasc. Res. 113 (2017) 1441–1452. doi:10.1093/cvr/cvx159.
[76] S.P.M. Janssen, G. Gayan-Ramirez, A. Van den Bergh, P. Herijgers, K. Maes, E. Verbeken, M. Decramer, Interleukin-6 causes myocardial failure and skeletal muscle atrophy in rats, Circulation. 111 (2005) 996–1005. doi:10.1161/01.CIR.0000156469.96135.0D.

[77] M.C. van de Veerdonk, H.J. Bogaard, N.F. Voelkel, The right ventricle and pulmonary hypertension, Heart Fail Rev. 21 (2016) 259–271. doi:10.1007/s10741-016-9526-y.
[78] C.E.E. van der Bruggen, R.J. Tedford, M.L. Handoko, J. van der Velden, F.S. de Man, RV pressure overload: from hypertrophy to failure, Cardiovasc. Res. 113 (2017) 1423–1432. doi:10.1093/cvr/cvx145.

Table 1 Echocardiographic parameters of RV and LV function in control rats and in rats after PH induction

	Control W1 (n=8)	MCT W1 (n=9)	Control W2 (n=8)	MCT W2 (n=9)	Control W3 (n=8)	MCT W3 (n=9)
HR (bpm)	359 ± 19	363 ± 15	394 ± 22	364 ± 10	365 ±22	359 ± 11
BW (g)	223.8 ± 9.3	189.2 ± 3.3	266.8 ± 13.4	215.9 ± 8.5 **	302.5 ± 16.2	256.3 ±6.0 *
Fulton index	0.24±0.02	0.27±0.01	0.24±0.01	0.36±0.002**	0.26±0.008	0.54±0.05***
PAAT (ms)	24.5 ± 2.1	33.6 ± 0.9	37.0 ± 0.8	25.1 ± 1.5 ***	39.3 ± 1.93	19.6 ± 1.7 ***
VTI pulmonary artery (mm)	4.97 ± 0.23	5.10 ± 0.20	5.70 ± 0.51	4.73 ± 0.36 ***	4.95 ± 0.53	3.07 ± 0.33 ***
RV EDd (mm)	3.6 ± 0.3	3.1 ± 0.2	3.5 ± 0.2	3.3 ± 0.3	3.2 ± 0.4	4.6 ± 0.4 **
RV EDs (mm)	2.2 ± 0.3	1.8 ± 0.1	2.4 ± 0.2	1.9 ± 0.1	2.5 ± 0.3	3.6 ± 0.4
RV thickness (mm)	1.14 ± 0.07	1.2 ± 0.11	1.12 ± 0.06	1.34 ± 0.07 *	1.25 ± 0.1	1.55 ± 0.06 **
RV FS (%)	40.4 ± 4.5	41.9 ± 3.4	38.2 ± 2.5	41.9 ± 2.4	39.9 ± 4.0	19.7 ± 7.5 **
VTI aorta (mm)	5.77 ± 0.45	6.22 ± 0.39	7.38 ± 0.46	6.46 ± 0.35	7.7 ± 0.17	5.66 ± 0.51 *
LV EDd (mm)	5.9 ± 0.2	5.7 ± 0.1	6.1 ± 0.4	6.0 ± 0.3	6.4 ± 0.2	4.4 ± 0.7 *
LV EDs (mm)	3.5 ± 0.3	3.1 ± 0.2	3.4 ± 0.2	3.2 ± 0.2	4.3 ± 0,1	2.4 ± 0.3 **
LV thickness (mm)	2.0 ± 0.1	1.6 ± 0.04	2.3 ± 0.2	1.9 ± 0.1	2.6 ± 0.1	2 ± 0.2 *
LV FS (%)	41.5 ± 3.7	45.9 ± 3.9	44.4 ± 3.5	45.9 ± 2.6	37.1 ± 2.2	40.4 ± 4.5
CO (mL)	71.2 ± 6.7	73.4 ± 8.8	108.2 ± 15.5	81.4 ± 5.6	127.4 ± 12.0	74.4 ± 3.8 **
Cardiac Index (mL/min/m^2)	324 ± 13	390 ± 48	410 ± 63	366 ± 22	354 ± 44	292 ± 18 *

Table 2 List of the gene expression assays (Life Technology) used in this study

Gene	Primer reference	Species
RYR2	Rn01470303_m1	Rat
SERCA2A	Rn00568762_m1	Rat
MYH6	Rn00691721_g1	Rat
MYH7	Rn01488777_g1	Rat
NPPB	Rn00580641_m1	Rat
NPPA	Rn00664637_g1	Rat
Col3a1	Rn01437681_m1	Rat
Col1a1	Rn01463848_m1	Rat

Table 3 List of the antibodies used in this study

Target	Antibody reference	Supplier
RYR2	MA3-916	ThermoFisher Scientific
SERCA2a	Sc-376235	SantaCruz Biotechnology
STIM1	SC6197	Sigma
STIM2	ACC-064	Alomone
Orai1	O8264	Sigma
Orai3	ACC-065	Alomone labs
TRPC1	Sc-133076	SantaCruz Biotechnology
TRPC3	ACC-016	Alomone labs
TRPC4	ACC-018	Alomone labs
TRPC5	ACC-020	Alomone labs
TRPC6	ACC-017	Alomone labs
IP3R2	ACC-116	Alomone labs
ET1RA	AER-001	Alomone labs
ET1RB	AER-002	Alomone labs
CD31	Ab81289	Abcam
CD34	ab81289	Abcam
CD45	610266	DB Transduction laboratories
GAPDH	AM4300	ThermoFisher Scientific
Total-PLB	Sc-21923	SantaCruz Biotechnology
S16 PLB	A010-12	Badrilla
T17 PLB	A010-13	Badrilla
Ser2808 RYR2	A010-31AP	Badrilla
Ser2814 RYR2	A010-30AP	Badrilla

Figure legends

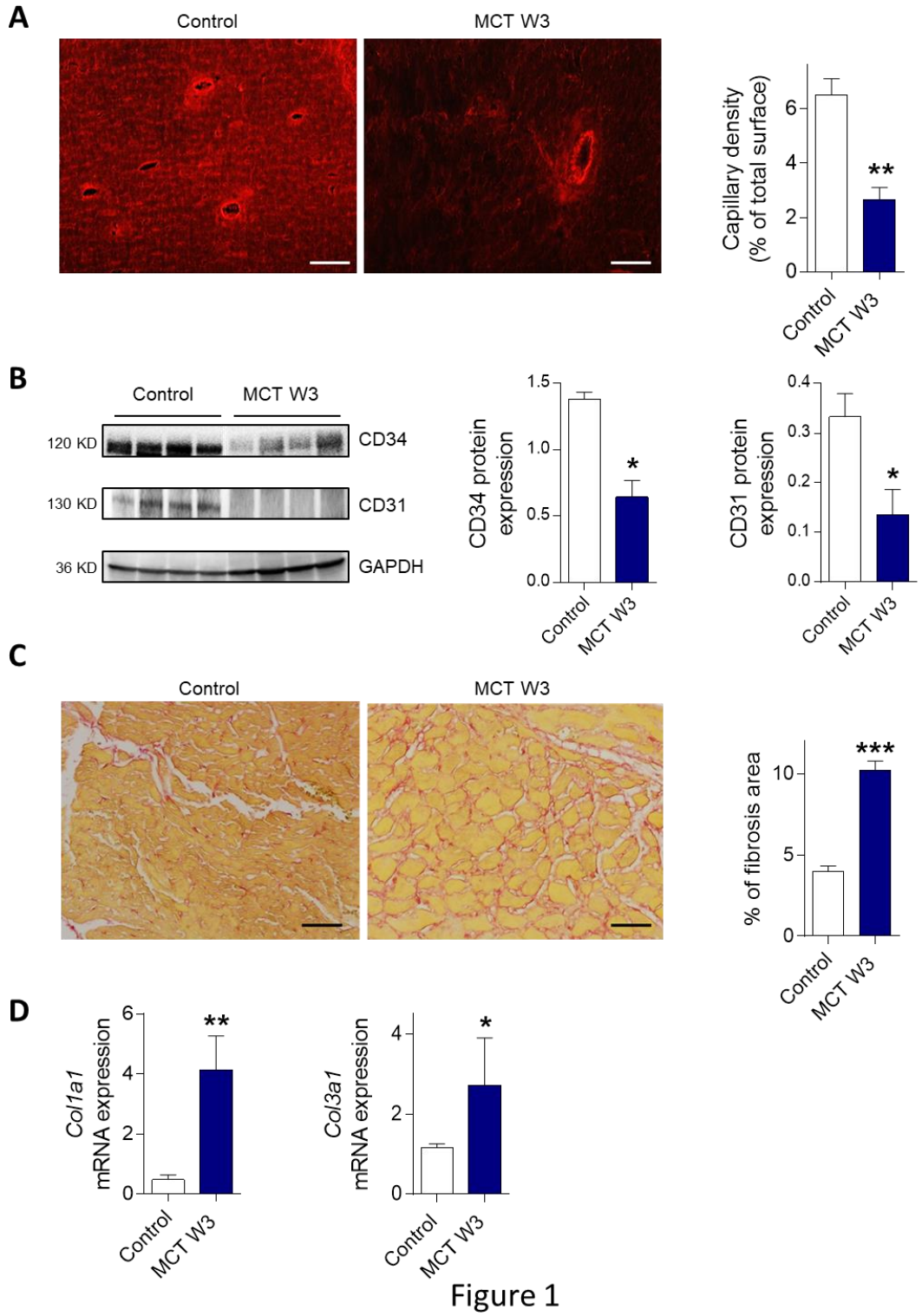

Figure 1

Fig. 1 RVH and RV dysfunction are associated with aberrant loss of capillarity density, fibrosis and inflammation. **a**, Left panel: immunostaining against the CD31 (red staining) in RV tissues from control rats and from MCT-exposed rats at W3 (n=3 rats). Scale bar, 50 µm. Right panel: quantification of capillary density by analysis of CD31 staining. **b**, Left panel: representative Western-blot of CD31 and CD34 protein expression in RV cardiomyocytes from control rats and from MCT-exposed rats at W3. Middle and right panels: quantification

of the relative expression of CD31 and CD34. GAPDH was used as the loading control (n=4 rats). **c**, Left panel: interstitial fibrosis identified with Sirius red staining in the RV compartments of control and MCT-exposed rats at W3. Right panel: quantification of the percentage of fibrosis in RV tissues from control and MCT-exposed rats (n=20 images per rat from 5 rats). **d**, mRNA expression of *Col3a1* and *Col1a1* in RV tissues isolated from control rats and MCT-exposed rats at W3 (n=4-5 rats).

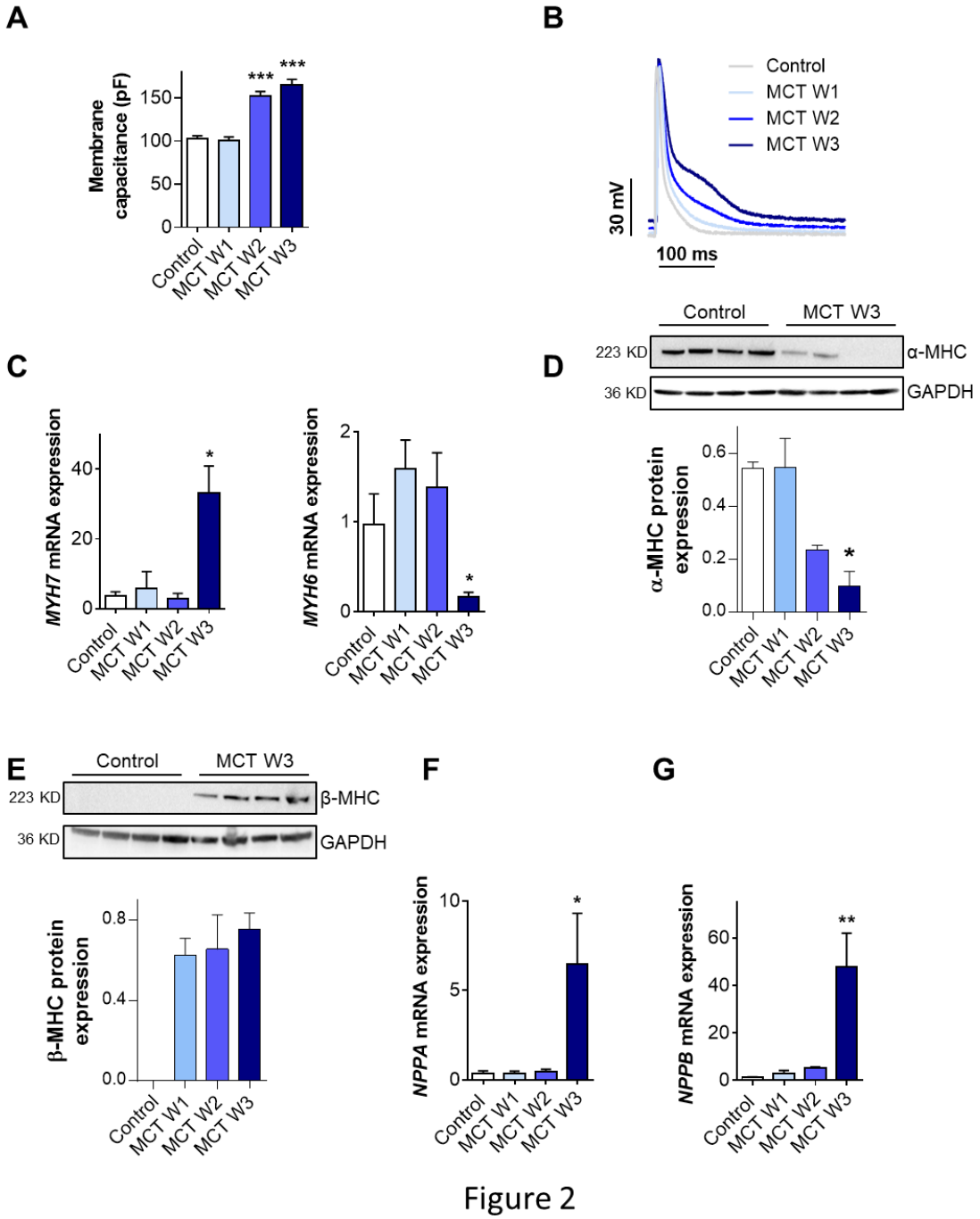

Figure 2

Fig. 2 *In vitro* characterization of RV dysfunction in the MCT-PH model. a, Cell capacitance of isolated RV cardiomyocytes from control rats and from MCT-treated rats 1 week (W1), two weeks (W2) and three weeks (W3) after exposure (n=5 rats, n=46-70 cells). **b**, Representative action potential (AP) in RV cardiomyocytes from control and MCT-exposed rats. **c**, mRNA expression of *MYH7* (left panel) and *MYH6* (right panel) (n=5-6 rats).

d-e, Top panels: representative Western-blots of α-MHC (**d**) and β-MHC (**e**) protein expression in RV cardiomyocytes from control and MCT-exposed rats. Bottom panels: quantification of the relative expression of α-MHC and β-MHC. GAPDH was used as the loading control (n=4 rats). **f-g,** mRNA expression of the *NPPA* (**f**) and *NPPB* (**g**) genes normalized by GAPDH mRNA in RV cardiomyocytes from control rats and from MCT rats (n=5-6 rats).

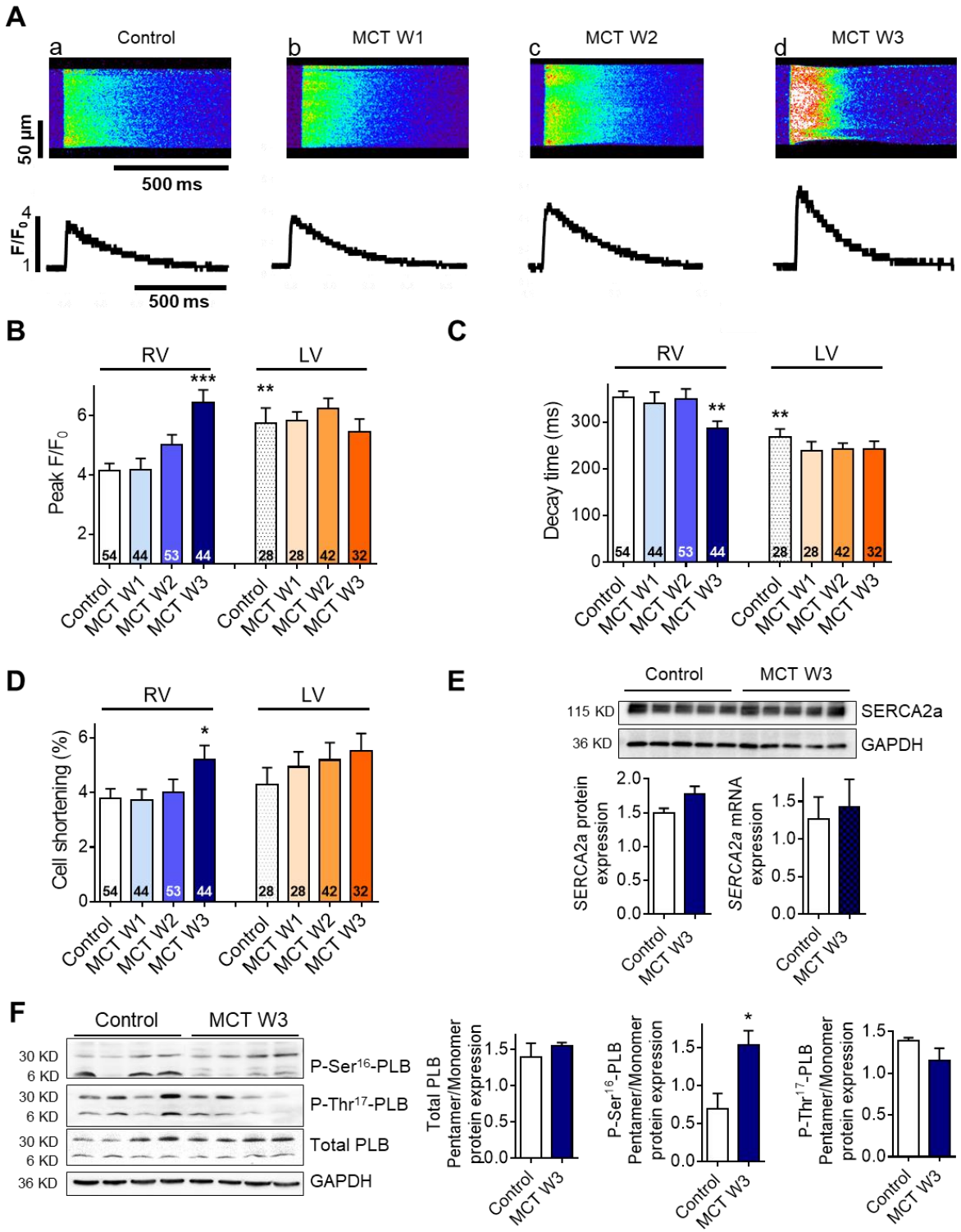

Figure 3

Fig. 3 Stimulated $[Ca^{2+}]_i$ transients in single RV and LV cardiomyocytes from MCT-PH rats. a, Top panel: line-scan of isolated RV cardiomyocytes loaded with Fluo-4/AM from control rats and from MCT-exposed rats (W1, W2 and W3). Bottom panel: corresponding traces of $[Ca^{2+}]_i$ transients. **b**, Amplitude of $[Ca^{2+}]_i$ transients (Peak F/F_0) obtained in RV and LV myocytes field-stimulated at 1 Hz from control and MCT-exposed rats. **c,** Average $[Ca^{2+}]_i$ transients decay time (ms) in RV and LV myocytes from control and MCT-exposed rats. **d**,

Average % of cell shortening in RV and LV myocytes from control and MCT-exposed rats. **e**, Representative western-blot and quantification of SERCA2a protein expression in RV cardiomyocytes from control and MCT-exposed rats (W3). GAPDH was used as the loading control (n=5 rats). Bottom panel: quantification of SERCA2a mRNA expression in RV cardiomyocytes from control and MCT-exposed rats (W3) normalized to the GAPDH mRNA level (n=4-5 rats). **f**, Representative western-blot and quantification of P-ser^{16}-PLB, P-ser^{17}-PLB, and total PLB expression in RV cardiomyocytes from control and MCT-exposed rats (W3). GAPDH was used as the loading control (n=4 rats).

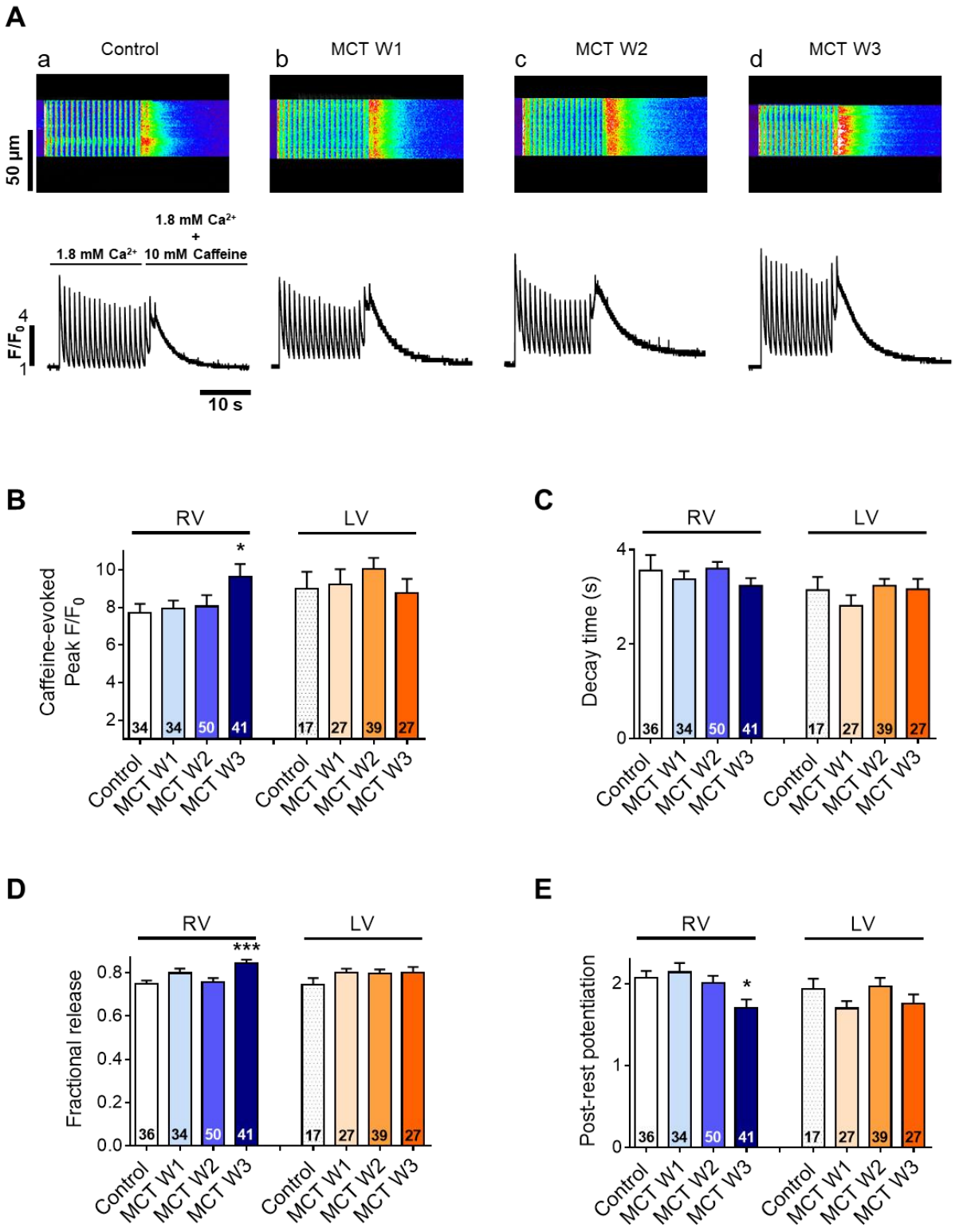

Figure 4

Fig. 4 Evaluation of the SR Ca^{2+} load in single RV and LV cardiomyocytes from MCT-PH rats. a, Top panel: line-scan of isolated RV cardiomyocytes loaded with Fluo-4/AM from control and MCT-exposed rats (W1, W2 and W3). Bottom panel: corresponding traces of caffeine-evoked $[Ca^{2+}]_i$ transients. **b**, Amplitude of the caffeine-evoked SR Ca^{2+} load (Peak F/F_0) recorded in RV and LV myocytes from control and MCT-exposed rats. **c,** Average caffeine-evoked SR Ca^{2+} load decay time in RV and LV myocytes from control and MCT-exposed rats. **d**, Average

fractional release in RV and LV myocytes from control and MCT-exposed rats. **e**, Average post-rest potentiation in RV and LV myocytes from control and MCT-exposed rats.

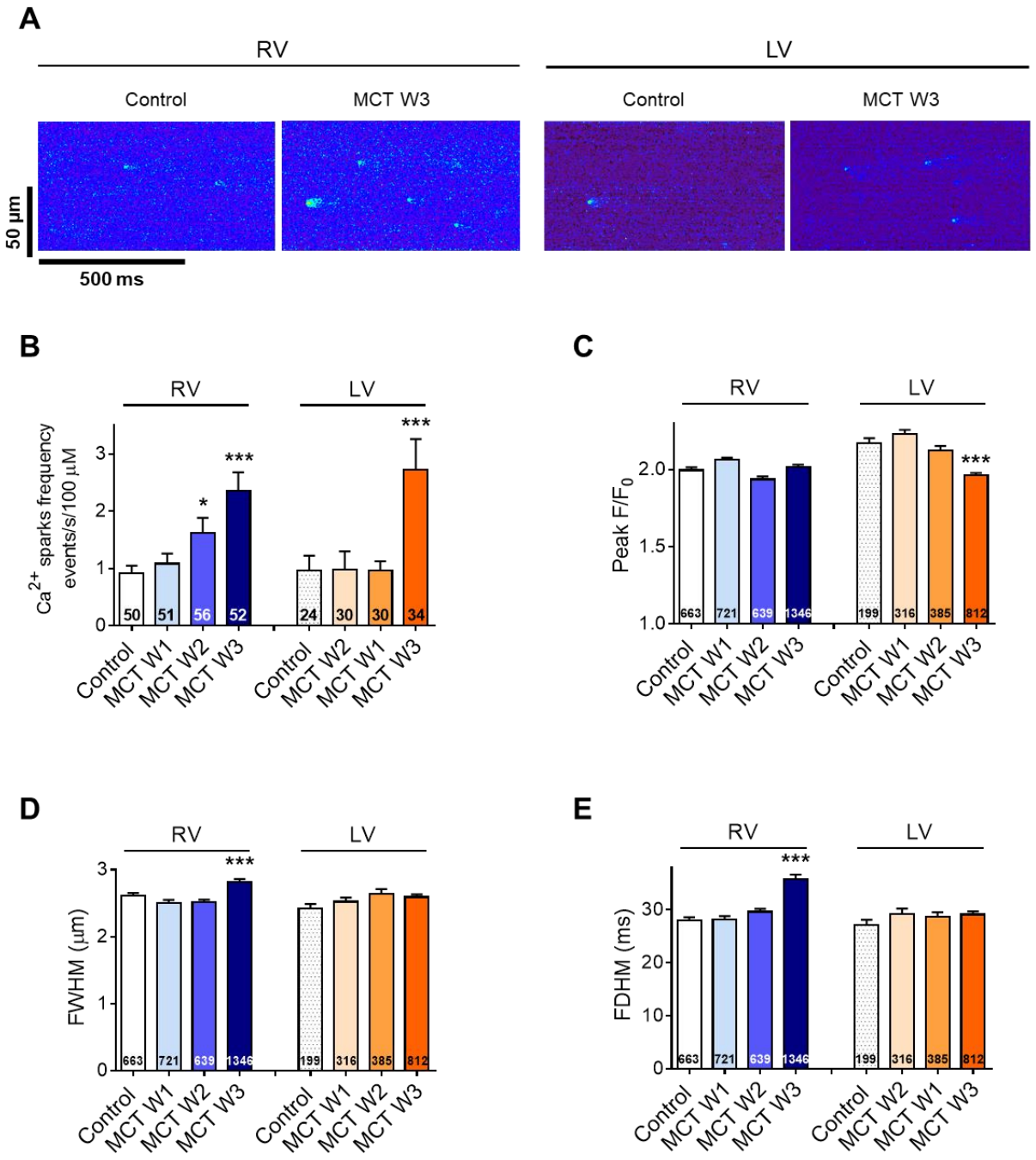

Figure 5

Fig. 5 Evaluation of Ca^{2+} spark frequency and properties in single RV and LV cardiomyocytes from MCT-PH rats. **a**, Line-scan images showing spontaneous Ca^{2+} sparks recorded in RV and LV cardiomyocytes from

control rats and from MCT-exposed rats at W3. **b**, Average Ca^{2+} spark frequency (events/s/100 µM) in RV and LV cardiomyocytes from control rats and from MCT-exposed rats at W3. **c**, Average Ca^{2+} spark amplitude (Peak F/F_0) in RV and LV myocytes from control and MCT-exposed rats. **d**, Average full width at half-maximum (FWHM) and **e**, full duration at half-maximum (FDHM) in LV and RV myocytes from control and MCT-exposed rats.

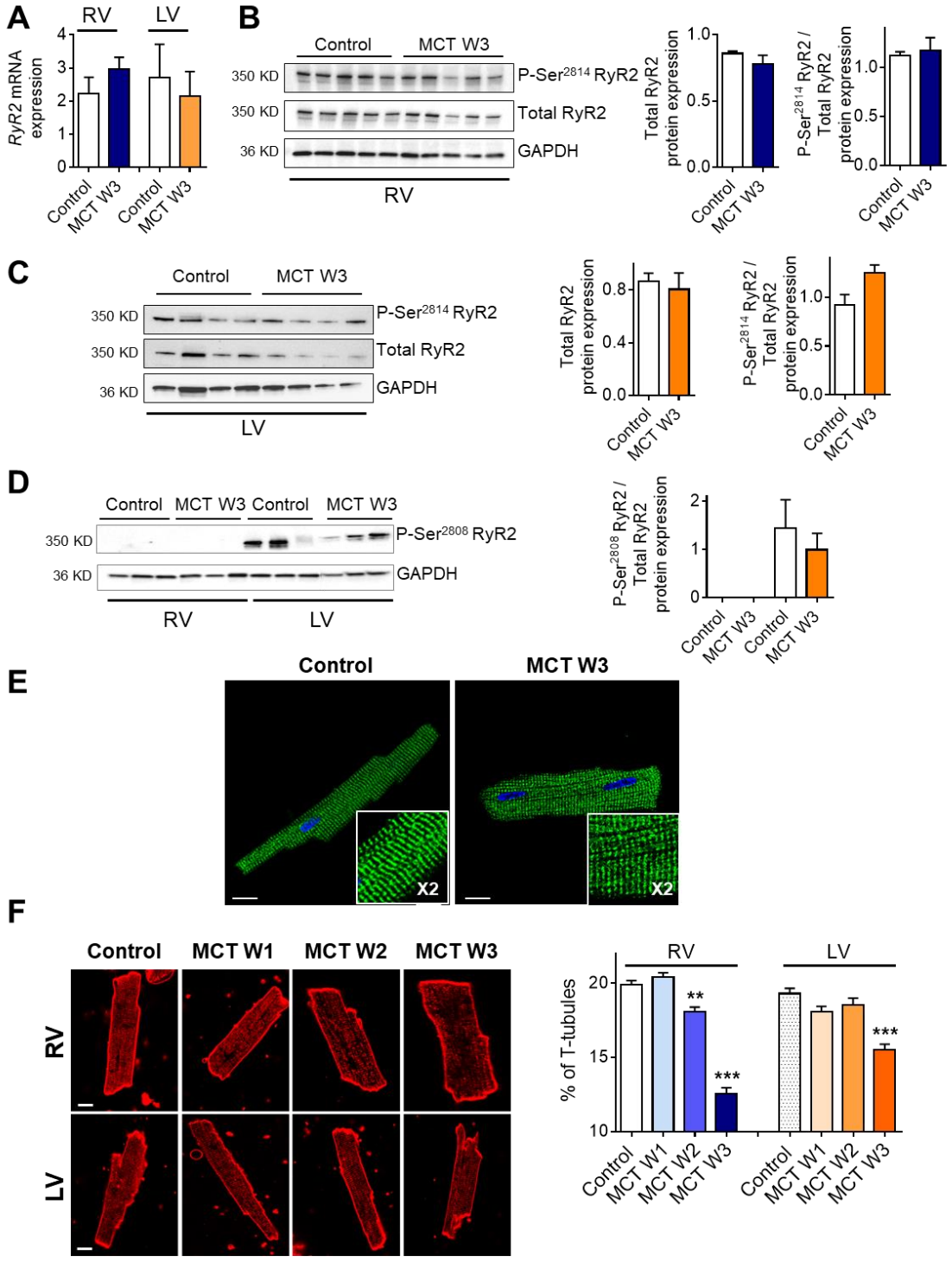

Fig. 6 Alterations of RyR organization and the T-Tubule network in RV and LV cardiomyocytes from MCT-PH rats. a, mRNA expression of RyR2 in RV and LV cardiomyocytes from control rats and from MCT-exposed

rats at W3 (n=4-6 rats). **b-c**, Representative western-blot of P-ser^{2814}-RyR2, and total-RyR2 expression in RV (B) and LV (C) cardiomyocytes from control and MCT-exposed rats (at W3). GAPDH was used as the loading control (n=4 rats). **d**, Representative western-blot of P-ser^{2808}-RyR2, and total-RyR2 expression in RV and LV cardiomyocytes from control and MCT-exposed rats (at W3). GAPDH was used as the loading control (n=4 rats). **e**, Immunolabeling and confocal images of RyR2 in RV cardiomyocytes from control and MCT-exposed rats (at W3). Scale bar, 10 μm. **f**, Analysis of T-tubule remodeling in MCT-exposed rats. Left panel, confocal images of the T-tubule network stained by Di-4ANEPPS in RV and LV cardiomyocytes from control and MCT-exposed rats during the progression of RV remodeling secondary to PH (n=65-150 cells). Scale bar, 10 μm. Right panel, average percentage of T-tubules under the cell surface in RV and LV cardiomyocytes from control and MCT-exposed rats.

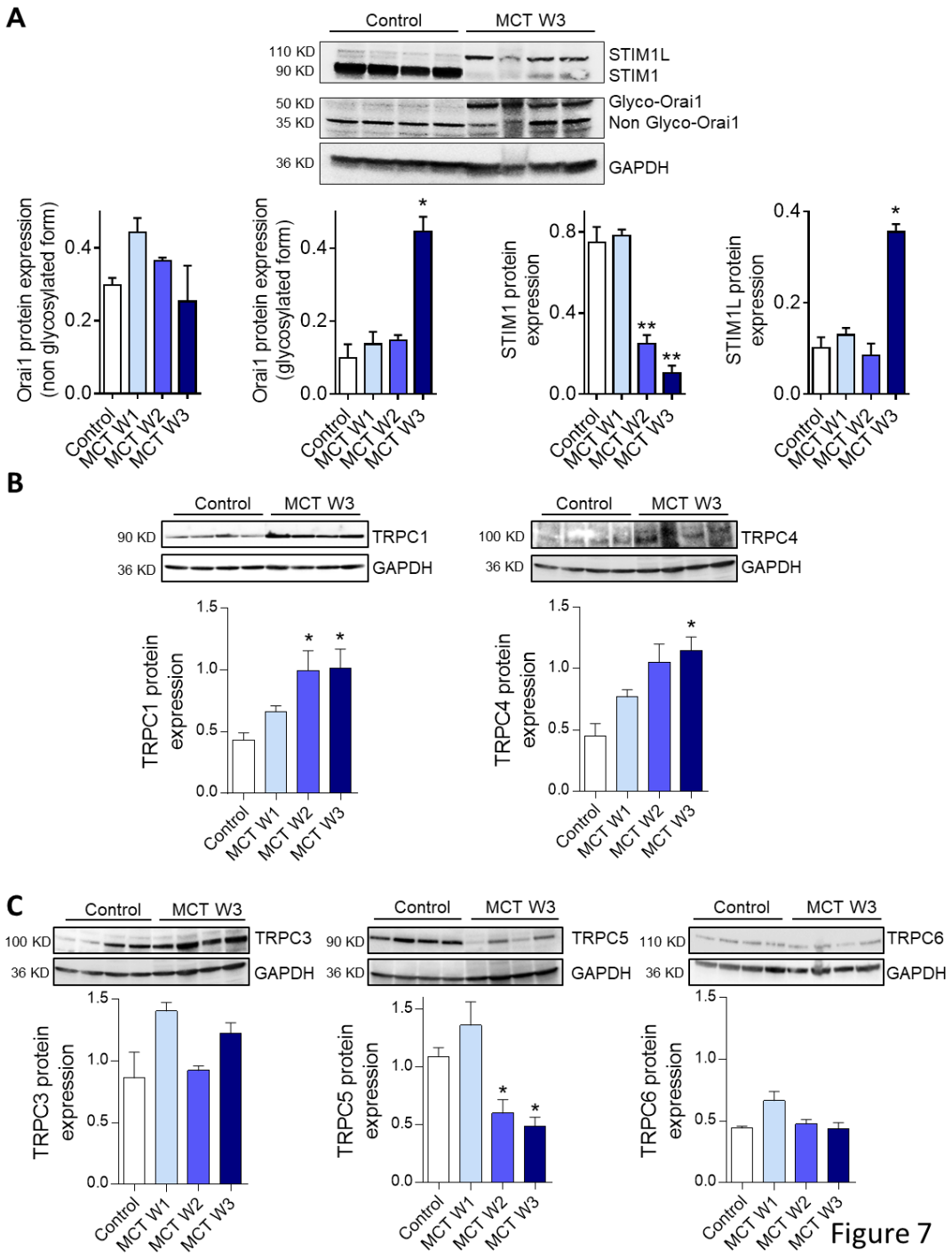

Fig. 7

Increased expression of STIM1L, glycosylated Orai1, TRPC1 and TRPC4 in hypertrophied RV myocytes. **a**, Top panel: representative western-blot of STIM1 and Orai1 protein expression in RV cardiomyocytes from control and MCT-exposed rats (W3). GAPDH was used as the loading control (n=4 rats). Bottom panel: quantification of the relative expression of non-glycosylated Orai1, glycosylated Orai1, classic STIM1 and the STIM1L isoform from control rats and from MCT-exposed rats at W1, W2 and W3. **b-c,** Top panel: representative Western-blot of TRPC1 (**b**), TRPC4 (**b**), TRPC3 (**c**), TRPC5 (**c**) and TRPC6 (**c**) protein expression in RV cardiomyocytes from control and MCT-exposed rats (W3). GAPDH was used as the loading control (n=4 rats). Bottom panel: quantification of the relative expression of the TRPC1, C4, C3, C5 and C6 isoforms from control and MCT-exposed rats at W1, W2 and W3.

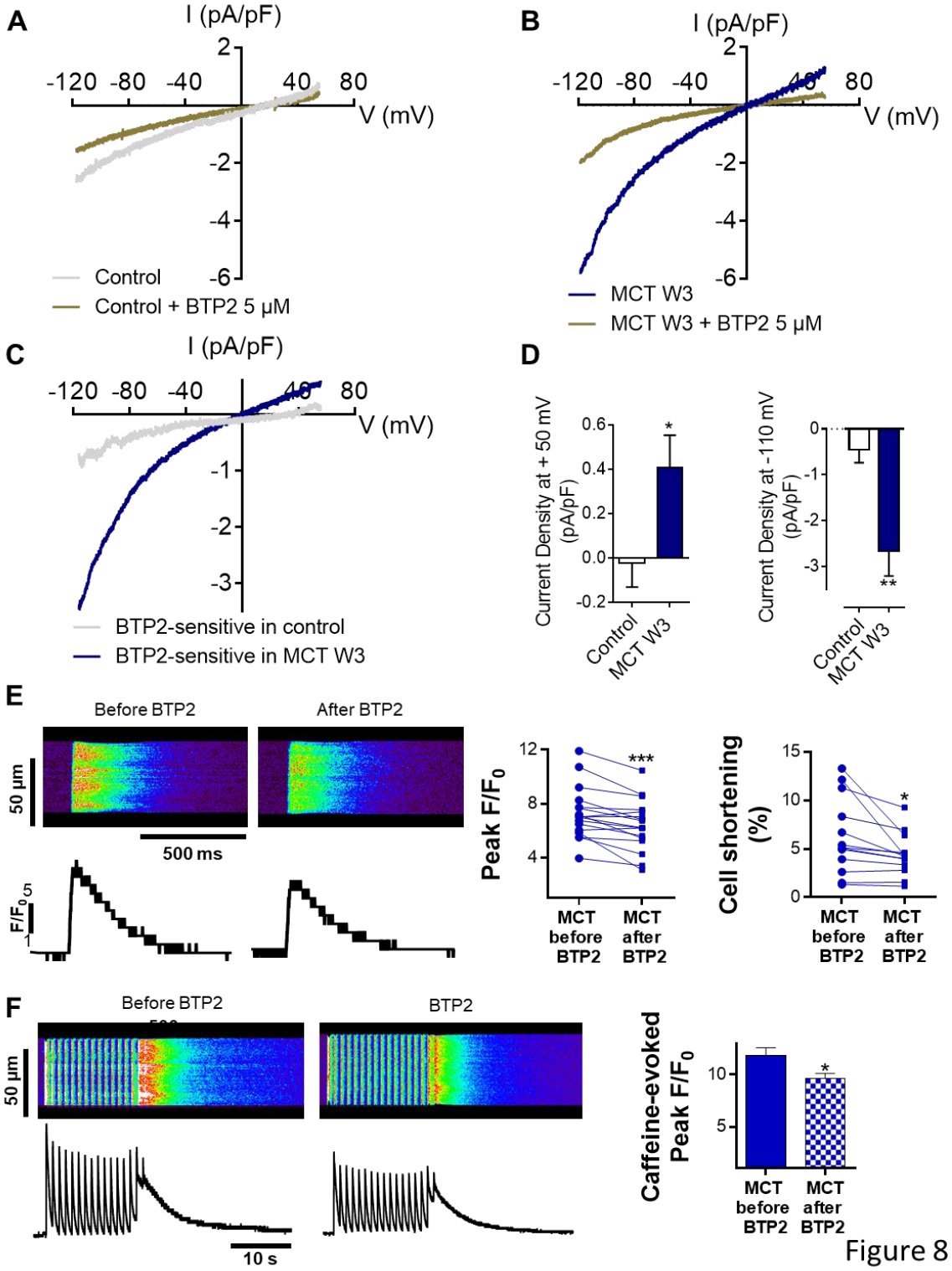

Figure 8

Fig. 8 I_{CRAC}-like current in single RV cardiomyocytes from MCT-PH rats. Whole-cell patch-clamp recordings in RV cardiomyocytes from control and MCT-exposed rats at W3 in the presence of L-type Ca^{2+} channels and Na/Ca^{2+} exchanger blockers (10 µM nifedipine and 5 µM KB-R7943). **a**, Representative I-V relationships elicited by a ramp voltage-clamp in RV cardiomyocytes from control rats in the presence or absence of 5 µM BTP2. **b**, Representative I-V relationships elicited by a ramp voltage-clamp in RV cardiomyocytes from MCT-exposed rats

at W3 in the presence or absence of BTP2. **c**, Representative I-V relationships of the BTP2-sensitive current elicited by a ramp voltage-clamp in RV cardiomyocytes from control and MCT-exposed rats (W3). **d**, Current density of the BTP2-sensitive outward current at +50 mV (left panel) and the BTP2-sensitive inward current at -110 mV (right panel) (n=6-7 cells, 3 rats). **e**, Left panel: line-scan of isolated RV cardiomyocytes loaded with Fluo-4/AM from MCT-exposed rats (W3) before and after the application of 5 µM of BTP2. Right panel: average amplitude of $[Ca^{2+}]_i$ transients (Peak F/F_0) and average % of cell shortening before and after BTP2 application in RV myocytes field-stimulated at 1 Hz from MCT-exposed rats at W3. **f**, Left panel: line-scan of isolated RV cardiomyocytes loaded with Fluo-4/AM from control and MCT-exposed rats (W3) in the presence or absence of 5 µM of BTP2. Right panel: average of amplitude of the caffeine-evoked SR Ca^{2+} load (Peak F/F_0) recorded in RV myocytes from MCT-exposed rats (n=4 rats).

Supplemental Figure legends

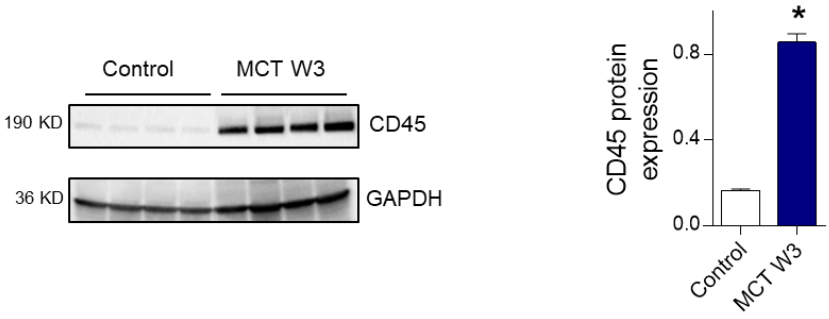

Supplemental Figure 1

Supplemental Fig. 1 Increased expression of CD45 (a pan leukocyte marker) in hypertrophied RV myocytes. Left panel: representative Western-blot of CD45 protein expression in RV tissues from control rats and from MCT-exposed rats at W3. GAPDH was used as the loading control (n=4 rats). Right panel, quantification of the relative expression of CD45 in myocytes from control rats and from MCT-exposed rats.

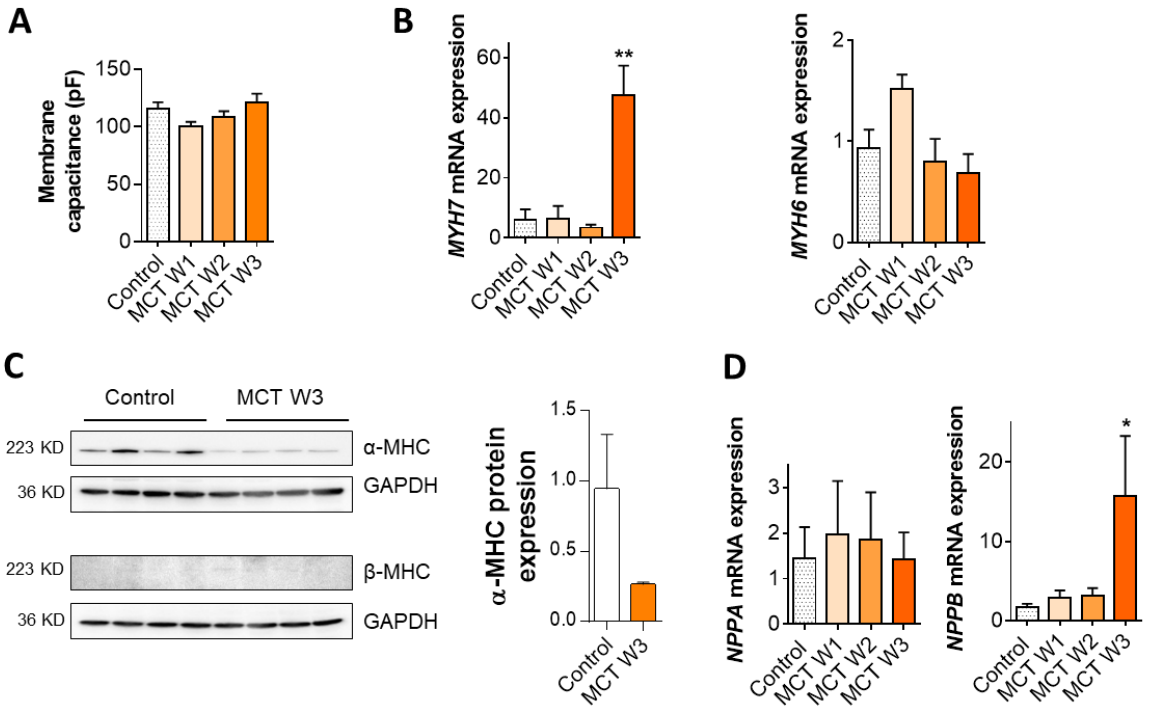

Supplemental Figure 2

Supplemental Fig. 2 *In vitro* characterization of LV function in the MCT-PH model. a, Cell capacitance of isolated LV cardiomyocytes from control and MCT-exposed rats (n=3 rats, n=21-32 cells). **b**, mRNA expression of the *MYH7* (left panel) and *MYH6* (right panel) genes in LV cardiomyocytes from control rats and MCT-exposed rats (n=5-6 rats). **c**, Left panel: representative Western-blot of α- and β-MHC protein expression in LV tissues from control and MCT-exposed rats at W3. GAPDH was used as the loading control (n=4 rats). Right panel, quantification of the relative expression of α-MHC in myocytes from control rats and from MCT-exposed rats at W3. **d**, mRNA expression of the *NPPA* (left panel) and *NPPB* (right panel) genes in LV cardiomyocytes from control rats and MCT rats (n=5-6 rats).

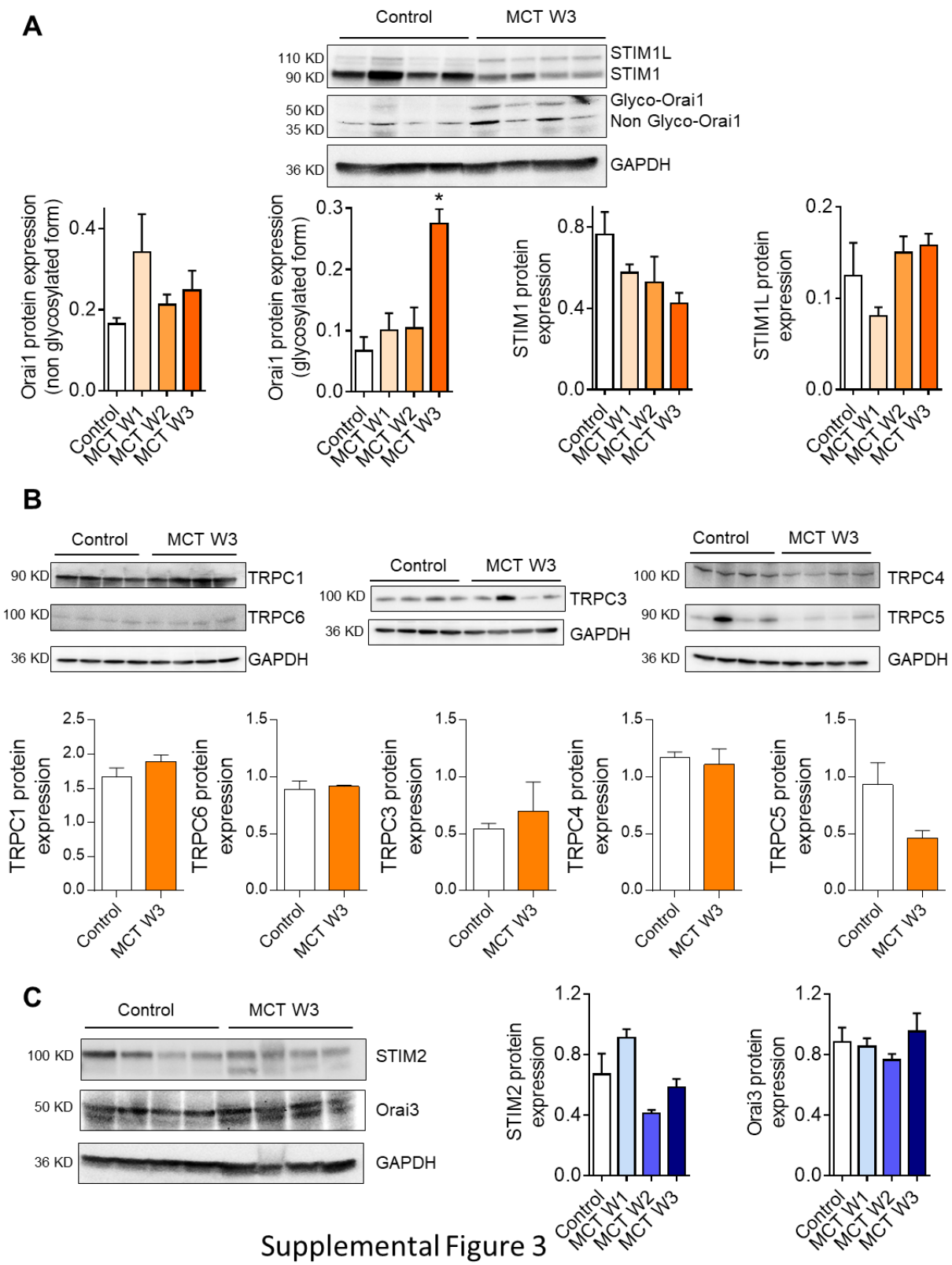

Supplemental Fig. 3 Unchanged expression of SOC molecules in LV cardiomyocytes from MCT-PH rats. a, Top panel: representative Western-blot of STIM1 and Orai1 protein expression in LV cardiomyocytes from control and MCT-exposed rats (W3). GAPDH was used as the loading control (n=4 rats). Bottom panel: quantification of the relative expression of non-glycosylated Orai1, glycosylated Orai1, classic STIM1 and the STIM1L isoform from control rats and from MCT-exposed rats at W1, W2 and W3. **b**, Top panel: representative Western-blot of

TRPC1, TRPC3, TRPC4, TRPC5 and TRPC6 protein expression in LV from control and MCT-exposed rats (W3). GAPDH was used as the loading control (n=4 rats). Bottom panel: quantification of the relative expression of the TRPC1, C3, C4, C5 and C6 isoforms in cardiomyocytes from control and MCT-exposed rats at W3. **c**, Left panel: representative Western-blot of STIM2 and Orai3 protein expression in LV cardiomyocytes from control and MCT-exposed rats (W3). GAPDH was used as the loading control. Right panel: quantification of the relative expression of Orai3 and STIM2 in RV from control rats and from MCT-exposed rats at W1, W2 and W3 (n=4 rats).

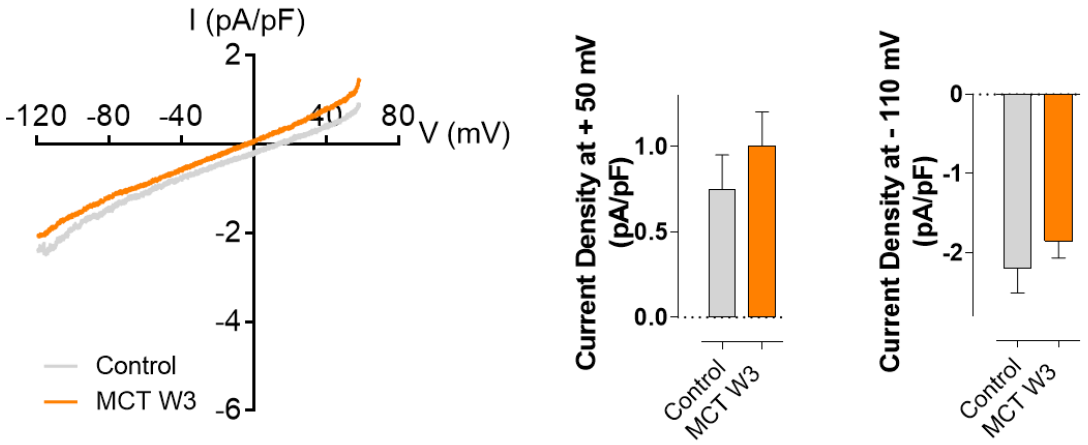

Supplemental Figure 4

Supplemental Fig. 4 Unchanged activity of SOC molecules in LV cardiomyocytes from MCT-PH rats. Left panel: representative I-V relationships elicited by a ramp voltage-clamp in LV cardiomyocytes from control and MCT-exposed rats (W3). Right panel: current density at +50 mV and current density at -110 mV in LV cardiomyocytes from control and MCT-exposed rats (W3). (n=4-5 cells).

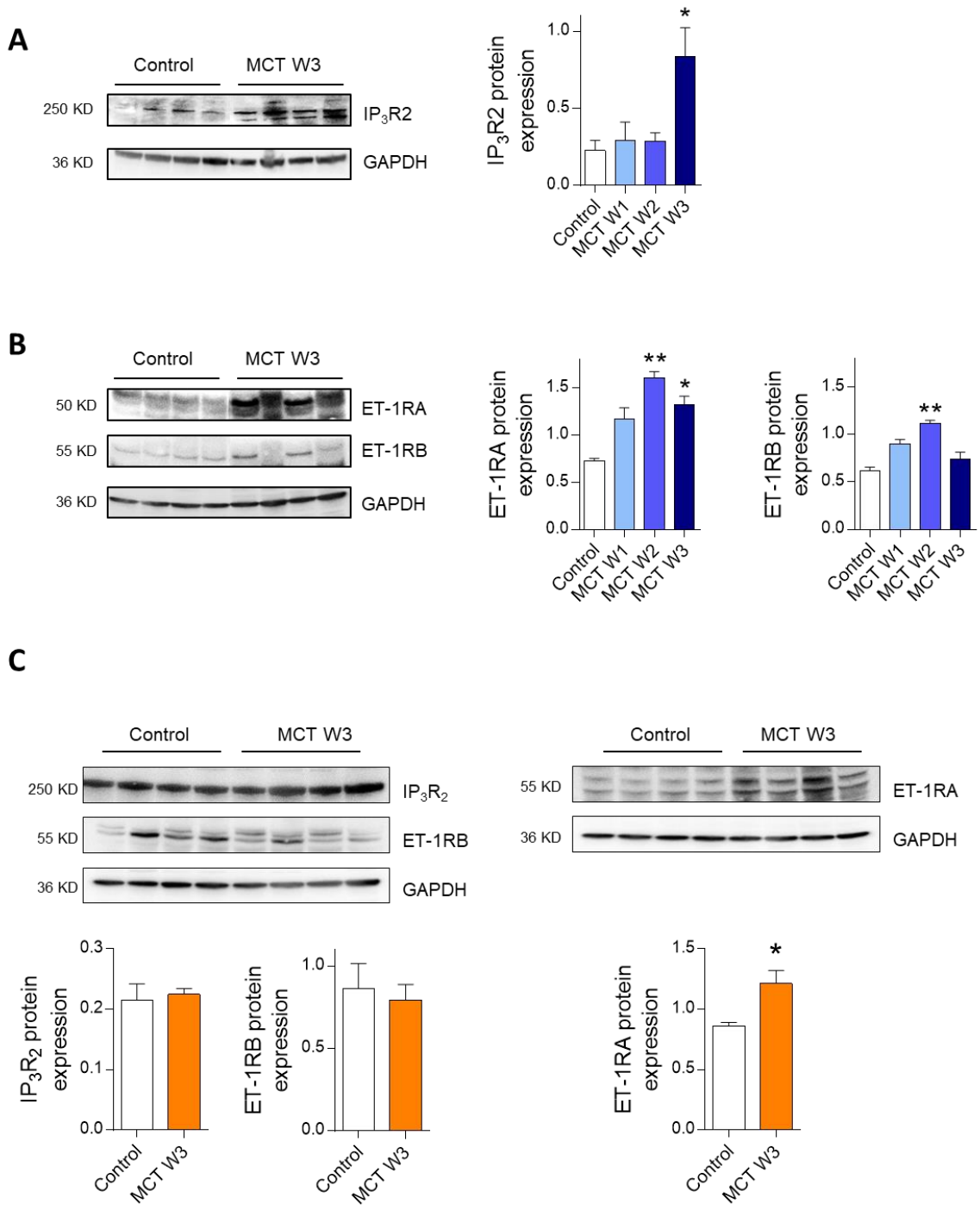

Supplemental Figure 5

Supplemental Fig. 5 Increased expression of IP_3R2 and endothelin-1 receptors in hypertrophied RV myocytes. a, Left panel: representative Western-blot of IP_3R2 protein expression in RV cardiomyocytes from control rats and from MCT-exposed rats at W3. GAPDH was used as the loading control (n=4 rats). Right panel: quantification of the relative expression of IP_3R2 from control rats and from MCT-exposed rats at W1, W2 and W3. **b**, Left panel: representative Western-blot of ET-1RA and ET-1RB protein expression in RV cardiomyocytes from control rats and from MCT-exposed rats at W3. GAPDH was used as the loading control (n=4 rats). Right

panel: quantification of the relative expression of ET-1RA and ET-1RB from control rats and from MCT-exposed rats at W1, W2 and W3. **c,** Top panel: representative Western-blot of IP_3R2, ET-1RA and ET-1RB protein expression in LV cardiomyocytes from control rats and from MCT-exposed rats at W3. GAPDH was used as the loading control (n=4 rats). Bottom panel: quantification of the relative expression of IP_3R2, ET-1RA and ET-1RB from control rats and from MCT-exposed rats at W3.